Blueprints of disease: precision platforms for modelling breast cancer

Lutz, C.

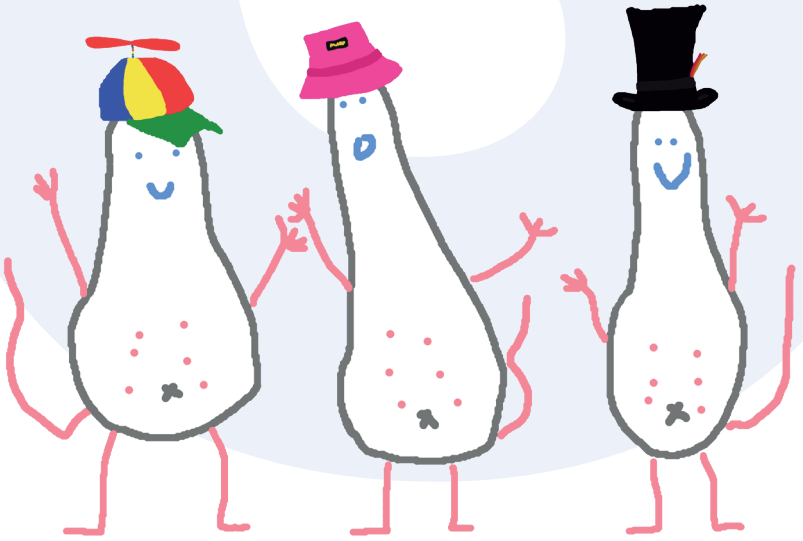

CHAPTER 6

Large-scale characterisation of orthotopic cell line-derived xenografts identifies TGF-β signalling as a key regulator of breast cancer morphology and aggressiveness

Catrin Lutz, Xue Chao, Bim de Klein, Jinhyuk Bhin, Madelon Badoux, Timo Eijkman, Apostolos P Nikolakopoulos, Stefan J Hutten, Natalie Proost, Bjørn Siteur, Marieke van de Ven, Ji-Ying Song, Jacco van Rheenen, Jessica Morgner, Stefan Prekovic & Jos Jonkers

Cancer Research. 2025 July 85 (14): 2608-2625

Abstract

Breast cancer (BC) is a heterogeneous disease with diverse morphological and molecular subtypes. Preclinical models that recapitulate the heterogeneity of human BC are needed to advance our fundamental understanding of what makes BC an aggressive disease. To study mechanisms underlying BC progression, we generated orthotopic cell line-derived xenograft (CDX) models from 20 different human BC cell lines using both mammary intraductal (MIND) injections and fat-pad transplantations (FPT). The resulting MIND-CDX and FPT-CDX models covered the full spectrum of disease progression, from *in situ* disease to metastatic growth. Pathological analysis revealed two distinct tumour growth morphologies, flat vs. nodular, and transcriptomics analysis identified the TGF-β pathway as a potential regulator of these two phenotypes in primary BC. Indeed, knockout of SMAD4 converted nodular-growing tumours to a more confined disease, while constitutively active TGFBR1 renders lesions more aggressive. This research not only offers insights into the factors driving BC morphology and aggressiveness but also establishes a comprehensive and valuable resource of well-characterised orthotopic CDX models for BC research.

Significance

Establishment and investigation of the largest collection of fully characterised breast cancer cell line xenograft models identifies key determinants of tumour morphology and aggressiveness and enables informed pre-clinical modelling for further research.

Introduction

Breast cancer (BC) is the most common cancer in women, with over 2.3 million new cases worldwide every year and incidences still rising [1]. BC comprises multiple clinical subtypes, each largely heterogeneous in morphology, oestrogen receptor (ER), progesterone receptor (PR) and human epidermal growth factor receptor 2 (HER2) status, gene expression profiles, DNA mutations, as well as in microenvironmental factors such as stromal involvement and immune cell status [2,3]. Thus, preclinical models that recapitulate the heterogeneity of human BC are required for basic and translational BC research.

Since the establishment of BT-20 cells in 1958 [4], a growing number of BC cell lines have been generated and used to study molecular tumour biology, test drug efficacy, and develop novel diagnostic tools for BC [5,6]. BC cell lines are commonly transplanted in immunodeficient mice and the resulting cell line-derived xenograft (CDX) models remain valuable assets in preclinical BC research [6-8]. However, despite availability of a wide array of published BC cell lines, most studies revert to a limited set of models that fail to recapitulate the heterogeneity of human BC. Indeed, only six models (MCF-7, MDA-MB-231, T-47D, SK-BR-3, MCF10A and MDA-MB-468) cover more than 90% of all studies employing BC cell lines, with a single model (MCF-7) covering more than half of all studies [9].

The validity of the CDX models is also determined by the transplantation site. The few large-scale approaches published to date have used non-orthotopic implantation of tumour cells under the skin or mammary fat-pad (FP), which does not mimic the tumour microenvironment in patients [10]. Orthotopic CDX models of BC may yield different results, depending on whether mammary intraductal (MIND) injections or fat-pad transplantations (FPT) are used. For example, Sflomos *et al.* reported that MIND-injection of ER^+ MCF-7 cells yields tumours that retain their luminal characteristics whereas FPT of the same cells drives basal differentiation and results in more mesenchymal tumours [11]. Hence, a comprehensive collection of well-characterised orthotopic MIND-CDX and FPT-CDX models of human BC would facilitate (*i*) informed decision making when choosing an appropriate model, (*ii*) studying the heterogeneity of BC in experimentally tractable models, and (*iii*) unravelling mechanisms underlying this heterogeneity through comparative analyses between models.

In this study, we generated and characterised a large panel of MIND-CDX and FPT-CDX models spanning all major BC subtypes, to create a resource that permits selection of the most appropriate model(s) to address a given research question. We determined tumour engraftment rates and latencies, metastatic potential, as well as histopathological and molecular characteristics of the tumour outgrowths. We additionally studied the effect of hormones on tumour growth and morphology. Finally, we identified two distinct tumour growth patterns and uncovered the TGF-β pathway as a regulator of primary tumour growth morphology and aggressiveness and provide mechanistic insights showing that TGF-β signalling acts in autocrine fashion in MIND models whilst FPT xenografts are further enhanced in modulating aggressive growth by paracrine signalling via the microenvironment.

Results

In vivo growth morphology of BC cells is determined by transplantation site

To study the effect of the microenvironment on BC growth and morphology, we established CDX models using two different orthotopic transplantation methods, i.e., cell injection into the mammary FP (fat-pad transplantation; FPT method) or the mammary duct (mammary intraductal; MIND method), resulting in exposure of BC cells to two distinct orthotopic environments with different tissue organization and cellular compositions. To cover the full spectrum of BC subtypes, we used a panel of 10 different human BC cell lines (SUM52PE, MCF-7, T-47D, Evsa-T, SK-BR-5, SUM149PT, MCF10DCIS.com, MDA-MB-231, SK-BR-7, SUM159PT) that differ in their hormone receptor (HR) and HER2 status, the original BC subtype and site from which they were derived, as well as their *in vitro* morphology. All 10 cell lines were subjected to cell line authentication and their HR and HER2 status was determined by immunofluorescence (IF) staining (Supplementary Table 1 and Supplementary **Figure 1A-C**) Although T-47D cells have been reported to be HER2-negative [7], they showed prominent HER2 expression as determined by IF (**Supplementary Figure 1A**).

We next injected all cell lines into female NOD-scid-IL2Rg^{null} (NSG) mice, using both the FPT and MIND methods, and characterised the tumour outgrowths (**Figure 1A, Supplementary Figure 1D**). Interestingly, while all 10 cell lines

developed round, nodular tumours in the FPT-CDX models (**Figure 1B**), we observed two distinct growth patterns in the MIND-CDX models. While 4/10 MIND-transplanted cell lines (MCF10DCIS.com, MDA-MB-231, SK-BR-7, SUM159PT) grew out as round, nodular tumours, 6/10 lines (SUM52PE, MCF-7, T-47D, Evsa-T, SK-BR-5, SUM149PT) formed flat tumours, filling the structure of the mammary gland (**Figure 1B-C**). Strikingly, all MIND-injected cell lines showed almost exclusively one of both growth patterns, which never arose in a mixed fashion. Microscopic analysis of the tumours revealed that the flat-growing tumours were mostly confined within the mammary epithelium, growing along the mammary ducts and side branches (**Figure 1C**, right panel). These tumours, up until end stage, inflated the branched ductal structure of the basement membrane-surrounded mammary epithelium. In contrast, nodular-growing tumours displayed expansive growth, presenting themselves as a solid tumour mass with invasive components into the surrounding mammary FP from an early stage onwards (**Figure 1C**, left panel).

One of the challenges of creating CDX models from human BC in mice, is the development of sarcomatoid tumours, which are mesenchymal and known to be of aggressive nature, possibly explaining the more aggressive growth of the nodular tumours in our study. However, HE staining of all tumours revealed that most cell lines consistently developed adenocarcinomas. Solely SUM159PT cells grew out as sarcomas when transplanted intraductally (86%), as well as 7% of MIND-transplanted MCF-7 tumours and 23% of FP-transplanted SUM52PE tumours (**Figure 1D**). Therefore, given that both flat- and nodular-growing tumours are mostly adenocarcinomas, we can exclude that sarcomatoid tumours underlie the nodular growth phenotype.

Since flat-growing tumours were only observed in the MIND-CDX models, we hypothesized that the confined environment of the mammary ducts might repress or delay tumour outgrowth. Interestingly, on the contrary, MIND-CDX tumours had a shorter tumour latency than the FPT-CDX tumours (**Figure 1E and Supplementary Figure 1E-F**). The MIND-CDX models also showed more consistent tumour latencies per cell line compared to the FPT-CDX models (**Figure 1E**). The MIND-CDX models showed a median tumour onset of 78 and 46 days for the flat-growing and nodular-growing tumours, respectively, whereas FPT-CDX tumours grew out in 64 days on average (**Supplementary Figure 1E**). Additionally, MIND and FPT engraftment rates were comparable for all 10 cell lines (**Supplementary Figure 1D**).

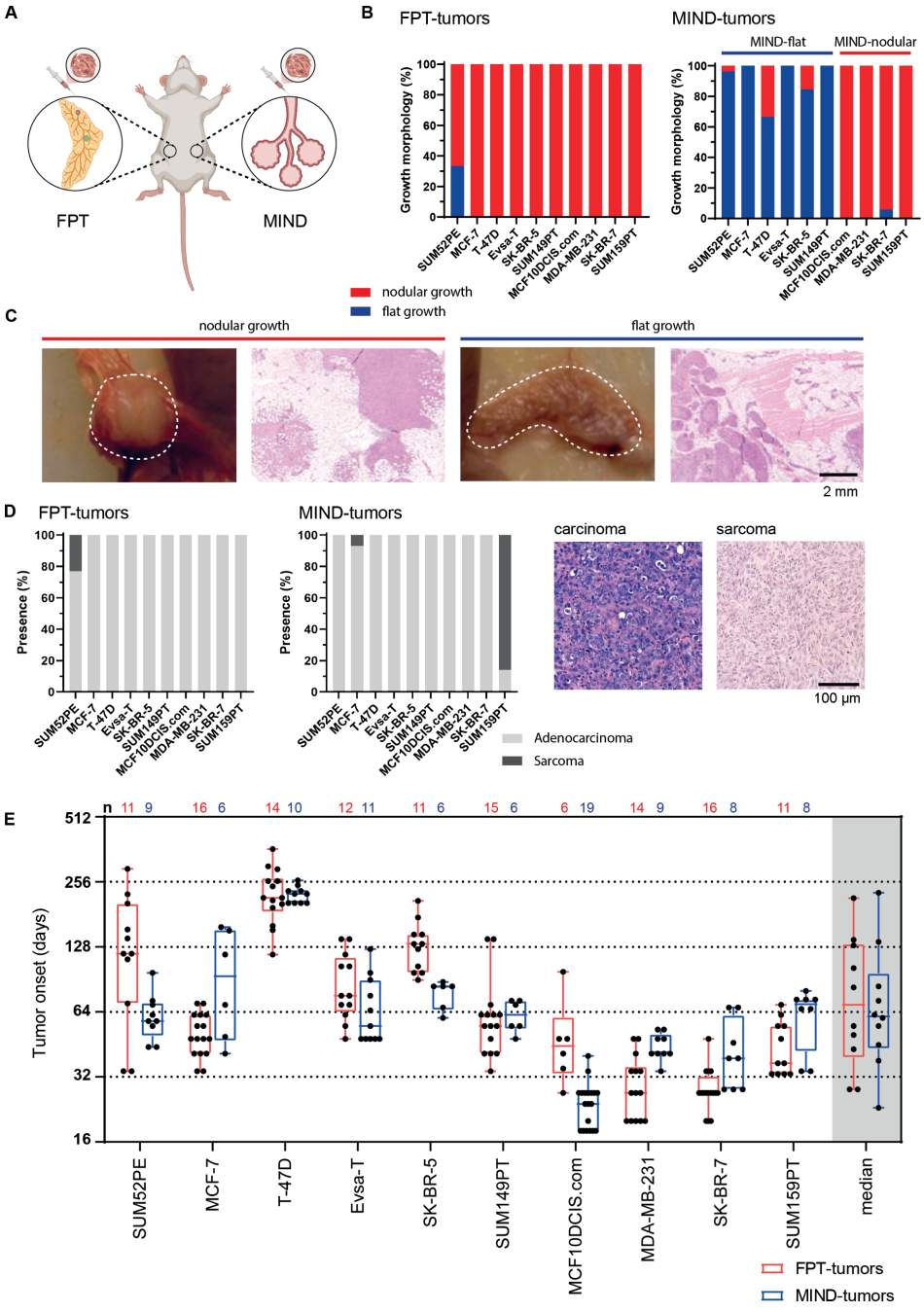
A
FPT
MIND
B
FPT-tumors
MIND-tumors
MIND-flat
MIND-nodular
Growth morphology (%)
SUM52PE
MCF-7
T-47D
Evsa-T
SK-BR-5
SUM149PT
MCF10DCIS.com
MDA-MB-231
SK-BR-7
SUM159PT
nodular growth
flat growth
C
nodular growth
flat growth
2 mm
D
FPT-tumors
MIND-tumors
Presence (%)
carcinoma
sarcoma
100 µm
Adenocarcinoma
Sarcoma
E
n 11 9 16 6 14 10 12 11 11 6 15 6 6 19 14 9 16 8 11 8
Tumor onset (days)
512
256
128
64
32
16
median
FPT-tumors
MIND-tumors

Figure 1: Morphology of BC cell line outgrowths is determined by transplantation site

A) Schematic of experimental set up showing that a panel of 10 BC cell lines were xenografted in NSG mice via two different methodologies: Fat-pad transplantation (FPT) or Mouse Intraductal injections (MIND). **B**) A panel of 10 different BC cell lines transplanted via the FPT method grew out as nodular tumours with the exception of SUM52PE which showed a flat tumour growth pattern in 33% (3/9) of outgrown tumours whilst 100% nodular tumours were observed for all other lines (MCF-7: 13/13, T-47D: 2/2, Evsa-T: 6/6, SK-BR-5: 13/13, SUM149PT: 11/11, MCF10DCIS.com: 2/2, MDA-MB-231: 11/11, SK-BR-7: 12/12, SUM159PT: 10/10). MIND-transplanted cells showed flat tumour growth for 6 (blue; SUM52PE (96%, 26/27), MCF-7 (100%, 17/17), T-47D (67%, 2/3), Evsa-T (100%, 18/18), SK-BR-5 (86%, 11/13), SUM149PT (100%, 9/9) and nodular tumour growth for 4 of the lines (red; MCF10DCIS.com (100%, 20/20), MDA-MB-231 (100%, 13/13), SK-BR-7 (94%, 16/17), SUM159PT (100%, 8/8)). **C**) Representative photographs of a MIND-nodular (red, left) or MIND-flat CDX tumour (blue, right) and their corresponding histology based on HE staining (scale bar 2 mm). **D**) Relative abundance (%) of FPT-CDX tumours (left) and MIND-CDX tumours (right) classified as adenocarcinomas (light grey) or sarcomas (dark grey). Most tumours are classified as adenocarcinomas, sarcomas are rarely detected. HE stained sections of a typical adenocarcinoma or sarcoma (far right, scale bar 100 µm). **E**) Tumour onset (days) of different BC CDX models. On average, cells show slower and more heterogeneous tumour outgrowth in FPT-CDX models (red) compared to MIND-CDX models (blue). Tumour onset of each respective tumour is depicted by a dot and earliest to latest onset (min to max data point) per model is highlighted by a box plot with median. Number of outgrown tumours per model is annotated above the graph and median tumour outgrowth per transplantation technique is shown on the far right (grey).

Taken together, we show that the conventional FPT method results in the uniform formation of nodular-shaped BC tumours (**Supplementary Figure 2**), whereas the MIND method results in tumours with a cell-line-specific and bimodal growth pattern, resulting in either MIND-nodular or MIND-flat tumours. Our results demonstrate that distinct cell lines produce tumours with a (nodular) growth pattern in a hard-wired, cell-intrinsic fashion that is not affected by the environment, whilst the growth morphology of other cell lines is strongly influenced by environmental factors.

Histopathological characterisation of MIND-CDX tumours

With the aim to create a well-documented resource and given the formation of the two distinct growth patterns, we set out to characterise the MIND-CDX tumours in more detail.

First, we scored HE-stained tumour sections for the presence of Ductal Carcinoma *in Situ* (DCIS) and/or Invasive Breast Cancer (IBC) lesions, which represent clinically relevant pathological hallmarks of BC invasiveness. DCIS lesions were present in all MIND-flat models but could only be identified in two of the MIND-nodular models, namely MCF10DCIS.com and SK-BR-7 (**Figure 2A+C**). This may indicate that the MIND-flat CDX tumours are indeed

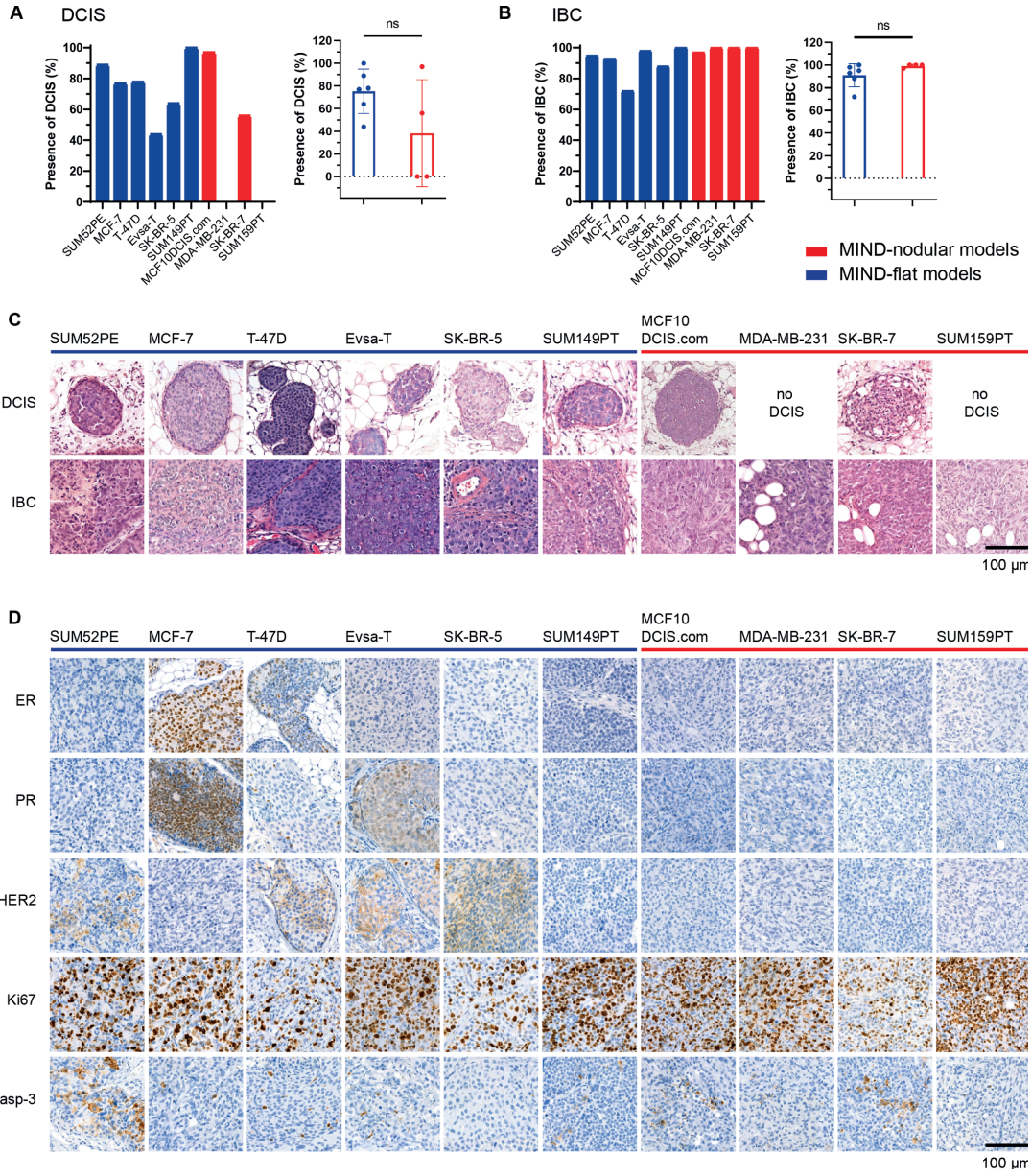
A
DCIS
Presence of DCIS (%)
SUM52PE
MCF-7
T-47D
Evsa-T
SK-BR-5
SUM149PT
MCF10DCIS.com
MDA-MB-231
SK-BR-7
SUM159PT
ns
B
IBC
Presence of IBC (%)
MIND-nodular models
MIND-flat models
C
DCIS
IBC
no DCIS
100 µm
D
ER
PR
HER2
Ki67
Casp-3
100 µm

Figure 2: Histopathological characterisation of MIND-CDX tumours

A) Relative abundance (%) of DCIS in MIND-flat (blue) and MIND-nodular (red) CDX tumours. DCIS is not detected in MIND-nodular CDX models of MDA-MB-231 and SUM159PT cells. Scoring is based on histology (ns=not significant, n=6 for MIND-flat and n=4 for MIND-nodular CDX tumour models, unpaired t-test). **B**) Relative abundance of IBC in MIND-flat (blue) and MIND-nodular (red) CDX models. Unlike DCIS, IBC is present in all MIND-CDX tumour models. Scoring is based on histology (ns=not significant, n=6 for MIND-flat and n=4 for MIND-nodular CDX tumour models, unpaired t-test). **C**) Examples of HE stainings for the basis of scoring histological features of DCIS and IBC in MIND-flat (blue) and MIND-nodular (red) CDX tumours (scale bar 100 µm). **D**) Immunohistochemical staining for tumour subtype (ER, PR, HER2), proliferation (Ki67) and apoptosis (Cleaved Caspase-3, Casp-3) in MIND-flat (blue) and MIND-nodular (red) CDX tumours (scale bar 100 µm).

more confined within the mammary epithelial structure resulting in more DCIS lesions. On the other hand, pathological features of IBC were present in all models, including both MIND-flat and -nodular tumours, ruling out IBC features as a determinant for the observed differences in growth morphology (**Figure 2B-C**).

Additionally, we performed an in-depth pathological characterisation of all tumours that arose from our models. Tumour grades and pathological growth features were assessed in DCIS (**Supplementary Figure 3A-B**) and IBC tumours (**Supplementary Figure 3C-D**). Furthermore, tumour differentiation, mitosis, fibrosis, inflammation, necrosis, calcifications, and the type of tumour margins were characterised by two independent, trained pathologists (**Supplementary Figure 3E-K**). Of note, none of these tumour features correlated with the flat or nodal growth morphologies.

Finally, we determined whether the expression status of ER, PR and HER2 persisted or changed upon *in vivo* tumour development. Immunohistochemistry (IHC) staining of ER, PR and HER2 revealed that all MIND-CDX tumours had retained receptor expression status of the cell lines, except for tumours from the (triple-positive) T-47D line, which lost PR-positivity in some cases (**Figure 2D, Supplementary Figure 4A**). Additionally, proliferation and apoptosis were assessed by IHC staining of Ki67 and cleaved caspase-3, respectively, showing high percentages of viable and proliferating cells in all tumours (**Figure 2D, Supplementary Figure 4A**). The same IHC stainings were performed for all FPT-CDX tumours, revealing overall high concordance between MIND-CDX tumours, FPT-CDX tumours and the corresponding cell lines (**Supplementary Figure 4B-C**).

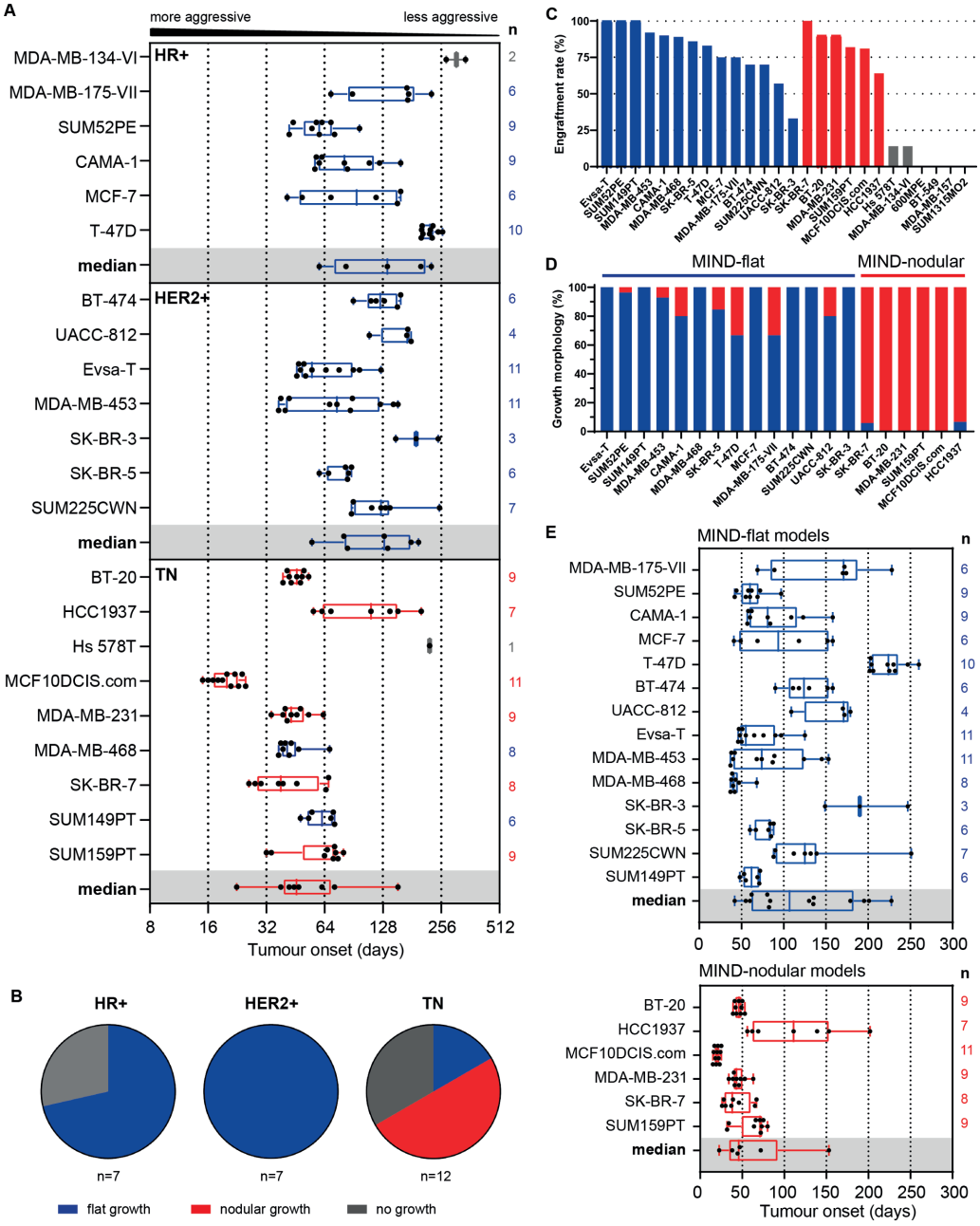
A
more aggressive
less aggressive
n
HR+
MDA-MB-134-VI 2
MDA-MB-175-VII 6
SUM52PE 9
CAMA-1 9
MCF-7 6
T-47D 10
median
HER2+
BT-474 6
UACC-812 4
Evsa-T 11
MDA-MB-453 11
SK-BR-3 3
SK-BR-5 6
SUM225CWN 7
median
TN
BT-20 9
HCC1937 7
Hs 578T 1
MCF10DCIS.com 11
MDA-MB-231 9
MDA-MB-468 8
SK-BR-7 8
SUM149PT 6
SUM159PT 9
median
8 16 32 64 128 256 512
Tumour onset (days)
B
HR+
HER2+
TN
n=7
n=7
n=12
flat growth
nodular growth
no growth
C
Engraftment rate (%)
100 75 50 25 0
Evsa-T SUM52PE SUM149PT MDA-MB-453 CAMA-1 MDA-MB-468 SK-BR-5 T-47D MCF-7 MDA-MB-175-VII BT-474 SUM225CWN UACC-812 SK-BR-3 SK-BR-7 BT-20 MDA-MB-231 SUM159PT MCF10DCIS.com HCC1937 Hs 578T MDA-MB-134-VI 600MPE BT-549 MDA-MB-157 SUM315MO2
D
MIND-flat
MIND-nodular
Growth morphology (%)
100 80 60 40 20 0
Evsa-T SUM52PE SUM149PT MDA-MB-453 CAMA-1 MDA-MB-468 SK-BR-5 T-47D MCF-7 MDA-MB-175-VII BT-474 SUM225CWN UACC-812 SK-BR-3 SK-BR-7 BT-20 MDA-MB-231 SUM159PT MCF10DCIS.com HCC1937
E
MIND-flat models
n
MDA-MB-175-VII 6
SUM52PE 9
CAMA-1 9
MCF-7 6
T-47D 10
BT-474 6
UACC-812 4
Evsa-T 11
MDA-MB-453 11
MDA-MB-468 8
SK-BR-3 3
SK-BR-5 6
SUM225CWN 7
SUM149PT 6
median
0 50 100 150 200 250 300
MIND-nodular models
n
BT-20 9
HCC1937 7
MCF10DCIS.com 11
MDA-MB-231 9
SK-BR-7 8
SUM159PT 9
median
0 50 100 150 200 250 300
Tumour onset (days)

Figure 3: MIND-CDX tumour growth morphology is independent of BC cell line subtype

A) Mammary tumour onset (days) of each respective tumour in MIND-CDX models grouped according to their HR^+, $HER2^+$ or Triple Negative (TN) subtype. Tumour onset is depicted by a dot and earliest to latest onset (min to max data point) per model is highlighted by a box plot with median. Number of outgrown tumours per model is annotated to the right of the graph and median tumour outgrowth per BC subtype is shown at bottom of each box (grey). **B**) Pie charts showing the outgrowths pattern and engraftment success of transplanted cell lines (blue: flat growth, red: nodular growth, grey: no tumour growth). **C**) Engraftment rates (%) per cell line and outgrowths pattern (blue: flat growth, red: nodular growth, grey: no tumour growth, missing bars: no engraftment) showing the differences in engraftment success. **D**) Growth morphology (% of outgrown tumours) of MIND xenografts. 14/20 cell lines grow flat whilst 6/20 grow nodular. MIND-flat models (blue): Evsa-T (100%, 18/18), SUM52PE (96%, 26/27), SUM149PT (100%, 9/9), MDA-MB-453 (93%, 13/14), CAMA-1 (80%, 8/10), MDA-MB-468 (100%, 7/7), SK-BR-5 (85%, 11/13), T-47D (67%, 2/3), MCF-7 (100%, 17/17), MDA-MB-175-VII (67%, 2/3), BT-474 (100%, 4/4), SUM225CWN (100%, 8/8), UACC-812 (80%, 4/5), SK-BR-3 (100%, 4/4). MIND-nodular models (red): SK-BR-7 (94%, 16/17), BT-20 (100%, 5/5), MDA-MB-231 (100%, 13/13), SUM159PT (100%, 8/8), MCF10DCIS.com (100%, 20/20), HCC1937 (93%, 14/15). **E**) Mammary tumour onset (days) of MIND-CDX models grouped according to their flat (upper panel) or nodular (lower panel) tumour growth pattern showing that flat tumour growth takes on average longer compared to MIND-nodular tumours. Tumour onset is depicted by a dot and earliest to latest onset (min to max data point) per model is highlighted by a box plot with median. Number of outgrown tumours per model is annotated to the right of the graph and median tumour outgrowth per growth pattern is shown at bottom of each box (grey).

MIND-CDX tumour growth morphology is independent of BC cell line subtype

After characterising the CDX models, we next sought to explore what might cause the two distinct tumour growth types. For this, we expanded our panel to a total of 26 different BC cell lines, comprising 6 HR-positive (600MPE, MDA-MB-134-VI, MDA-MB-175-VII, CAMA-1, MCF-7, T-47D), 8 HER2-positive (SUM52PE, BT-474, UACC-812, Evsa-T, MDA-MB-453, SK-BR-3, SK-BR-5, SUM225CWN) and 12 triple-negative lines (BT-20, BT-549, HCC1937, Hs 578T, MCF10DCIS.com, MDA-MB-157, MDA-MB-231, MDA-MB-468, SK-BR-7, SUM1315MO2, SUM149PT, SUM159PT) (Supplementary Table 1). All cell lines were transduced with luciferase-encoding lentivirus to enable non-invasive, longitudinal monitoring of tumour growth and morphology via *in vivo* bioluminescence imaging (BLI).

The luciferase-expressing cell lines were transplanted via the MIND method and tumour growth pattern, engraftment rates and latencies were determined (**Figure 3, Supplementary Figure 5A-B**). Six of the 26 cell lines could not be included for further analysis due to a low engraftment rate (Hs 578T, HCC1937) or lack of engraftment (600MPE, BT-549, MDA-MB-157, SUM1315MO2) following MIND injection (**Figure 3C, Supplementary Figure 5A**).

In line with previous observations, BLI showed that MIND-CDX tumours from some cell lines grew out along the lengths of the mammary gland whilst staying in a flat shape, whereas other cell lines developed as nodular tumours (**Figure 3D, Supplementary Figure 6 and 7**). Notably, all MIND-nodular CDX tumours originated from triple-negative cell lines, while MIND-flat tumours originated from HR^+ or $HER2^+$ cell lines, indicating that HR status may indeed determine *in vivo* growth pattern (**Figure 3A-B**). However, with the extended panel of cell lines, we found two triple-negative cell lines (MDA-MB-468 and SUM149PT) developing as flat tumours. Therefore, although HR status may play a role in determining growth pattern, it is not the exclusive determinant.

Unsurprisingly, MIND-nodular triple-negative tumours grew faster than the MIND-flat tumours, within on average 46 days versus 78 days post injection, respectively (**Figure 3E, Supplementary Figure 5B**). When analysed by BC subtype, HR^+ and $HER2^+$ tumours grew out with variable latencies, ranging from 55 to 228 days. However, triple-negative cell lines developed tumours much faster, within 23 to 72 days, with an exceptional 153 days for HCC1937 (**Figure 3A**). This reflects the more aggressive nature of triple-negative BCs as seen in patients.

Taken together, MIND modelling of our extended panel confirmed the consistent and cell line-specific bimodal growth pattern of MIND-CDX tumours, with MIND-flat tumours arising mostly, but not exclusively, from HR^+ and $HER2^+$ cell lines.

MIND-tumours from MIND-nodular CDX models have increased metastatic potential

We next aimed to determine the metastatic potential of our MIND-CDX models and wondered whether the observed growth patterns held predictive value. Therefore, we transplanted our initial panel of 10 cell lines using the MIND method, removed the primary tumour at a size of 500 mm^3 and monitored subsequent metastatic growth using *in vivo* BLI until the set humane endpoints were reached (**Figure 4A, Supplementary Figure 8A**). Overall, metastases in one or multiple organs were observed in 50% of the transplanted cell lines, including three MIND-nodular (SK-BR-7, MDA-MB-231, SUM159PT) and two MIND-flat models (SUM52PE, Evsa-T) (**Figure 4B-C, Supplementary Figure 8B**). Several metastatic sites (most notably lung, heart and ovary) were shared amongst different cell line models. However, we could not detect any distinct pattern for metastatic routes, as both lympho- and hemangio-vascular

systems were involved (**Figure 4B**). Nevertheless, metastasis formation was more prominent, faster, and more widespread in MIND-nodular models compared to MIND-flat models (**Figure 4B-C and Supplementary Figure 8B-E**). The increased metastatic potential was observed despite the fact that MIND-nodular tumours were excised sooner than MIND-flat tumours due to their growth speed (**Figure 4D, Supplementary Figure 8D**). These data underscore the aggressive nature of the MIND-nodular models in the context of recurrence and metastasis formation. Notably, SK-BR-7 showed very high metastatic potential with recurrences arising in 11 out of 14 organs analysed, highlighting the utility of this model for studying triple-negative BC metastasis (**Figure 4B, D-E**).

We next asked whether non-metastatic cell lines had a decreased ability to disseminate from the primary tumour and invade into lymphatic or blood vessels. Therefore, we scored lymph-vascular invasion events based on the identification of single tumour cells or small cell clusters in lymphatic or blood vessels, as detectable on HE stained tumour sections (**Supplementary Figure 8C**, right image). We identified tumour cells in vessels in 2 out of 5 metastatic MIND-CDX models (Evsa-T and SK-BR-7), but also in the non-metastatic MCF-7, SK-BR-5 and MFC10DCIS.com models. Conversely, we did not observe disseminating tumour cells in the metastatic SUM52PE, MDA-MD-231 and SUM159PT models (**Figure 4B and Supplementary Figure 8C**). This implies that lymph-vascular invasion is a poor predictor of metastatic potential.

Altogether, we provide a detailed overview of the metastatic potential from a panel of 10 different MIND-CDX models, revealing that MIND-nodular tumours metastasize faster and with higher incidence.

Oestrogen influences growth kinetics but not morphology of MIND-CDX tumours

Although hormone receptor positivity did not strictly correlate with flat tumour growth, we sought out to explore whether hormone signalling does affect tumour growth morphology, especially since all HR^+ cell lines yielded MIND-flat tumours and none of the MIND-nodular models were HR^+.

To this end, we tested the effects of hormone-deprivation via ovariectomy (OVX) and/or oestrogen (E2) supplementation on the growth of MIND-CDX tumours. MIND transplantation experiments were performed with two MIND-flat ER^+ cell lines (MCF-7, MDA-MB-175-VII) and two MIND-nodular triple-

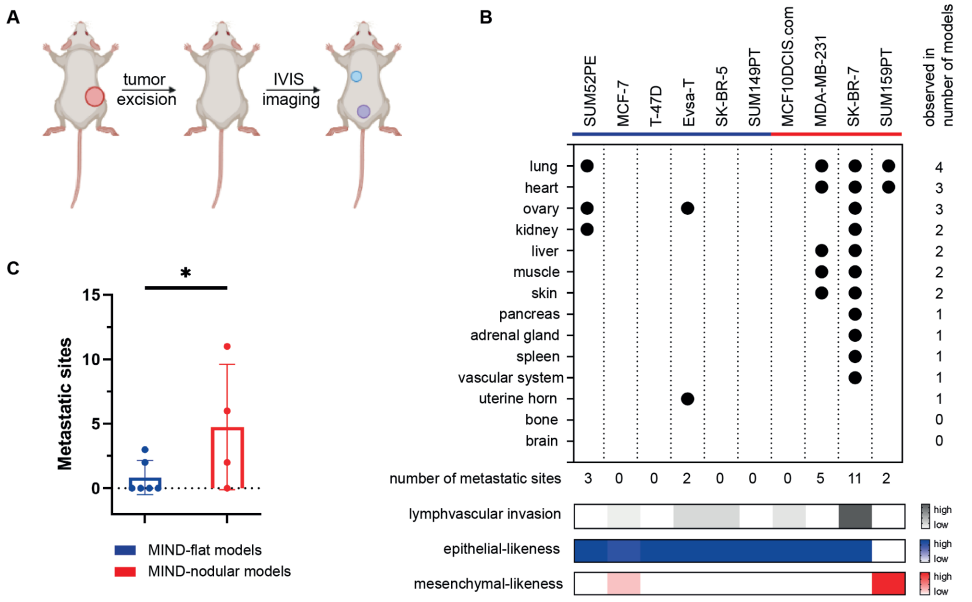
A
tumor excision
IVIS imaging
B
SUM52PE
MCF-7
T-47D
Evsa-T
SK-BR-5
SUM149PT
MCF10DCIS.com
MDA-MB-231
SK-BR-7
SUM159PT
observed in number of models
lung 4
heart 3
ovary 3
kidney 2
liver 2
muscle 2
skin 2
pancreas 1
adrenal gland 1
spleen 1
vascular system 1
uterine horn 1
bone 0
brain 0
number of metastatic sites 3 0 0 2 0 0 0 5 11 2
lymphvascular invasion
epithelial-likeness
mesenchymal-likeness
high
low
C
Metastatic sites
MIND-flat models
MIND-nodular models
D
SUM52PE
Radiance
Time (days)
SK-BR-7
Radiance
Time (days)
E
SUM52PE
lung
ovary
kidney
100 µm
SK-BR-7
lung
heart
ovary
kidney
liver
muscle
pancreas
skin
adrenal gland
spleen
vascular system
100 µm

Figure 4: MIND-tumours from MIND-nodular CDX models have increased metastatic potential

A) Experimental scheme of following metastasis formation in MIND-CDX models. After surgical removal of the primary tumour, tumour re-growth and metastasis formation was monitored by bioluminescence imaging. **B**) MIND-flat CDX tumour models (blue) harbour less metastatic organ sites than MIND-nodular models, including the most aggressive cell line SK-BR-7. Number of metastatic sites is depicted below the graph per cell line model. The number of models in which metastases were observed per organ is depicted on the right side of the graph. According to the presence of tumour cells in the lymph-vascular system, lymph-vascular invasion was scored and depicted in the grey bar for each cell line. Blue and red bars show epithelial-likeness and mesenchymal-likeness of the primary tumours respectively based on pathological assessment. **C**) Quantification of the number of metastatic sites from MIND-flat (blue bar) and MIND-nodular (red bar) CDX tumour models, showing more metastatic sites deriving from MIND-nodular models, underscoring the more aggressive nature of those models ($p=0.0160$, $n=6$ for MIND-flat and $n=4$ for MIND-nodular CDX tumour models, unpaired t-test). **D**) Example for metastatic growth speed of MIND-flat CDX tumours from SUM52PE cells (upper panel) and MIND-nodular CDX tumours from SK-BR-7 cells. Both cell lines show a very reproducible pattern of metastasis in terms of metastasis onset and growth speed. **E**) Representative HE stainings from metastatic sites of MIND-flat SUM52PE CDX tumours (lung, kidney, ovary) and from MIND-nodular SK-BR-7 CDX tumours (lung, kidney, heart, ovary, pancreas, liver, spleen, adrenal gland, vascular system, muscle, skin) (scale bars 100 µm).

negative cell lines (MDA-MB-231, MCF10DCIS.com) since TNBC tumours can show responses to hormones via paracrine mechanisms [12]. All 4 cell lines were injected in mice that were either supplemented with E2 or deprived thereof by means of OVX. As a control, mice were injected that underwent a sham operation (Sham OVX). To assess the effect of exogenous vs endogenous E2, we also supplemented OVX and Sham OVX animals with E2.

Interestingly, irrespective of presence or absence of E2, no change in growth pattern was observed for all cell lines and their morphology remained identical to what was observed previously (**Figure 5A-B and Supplementary Figure 9A-B**). This indicates that ER activity does not directly impact tumour growth morphology, underlining that receptor expression indeed correlates with, but does not underlie, BC tumour growth morphology. In E2-depleted mice, tumour onset was substantially delayed for the ER^+ MCF-7 and MDA-MB-175-VII cell lines. E2-supplemented mice showed faster tumour growth than the non-supplemented groups, irrespective of OVX status. Growth of the triple-negative MDA-MB-231 and MCF10DCIS.com cell lines was not delayed by E2-depletion (OVX vs Sham OVX) and only modestly accelerated by E2-supplementation (**Figure 5C and Supplementary Figure 9C**). Altogether, hormonal perturbations affected growth kinetics of HR^+ CDX tumours, but not tumour growth morphology in MIND models.

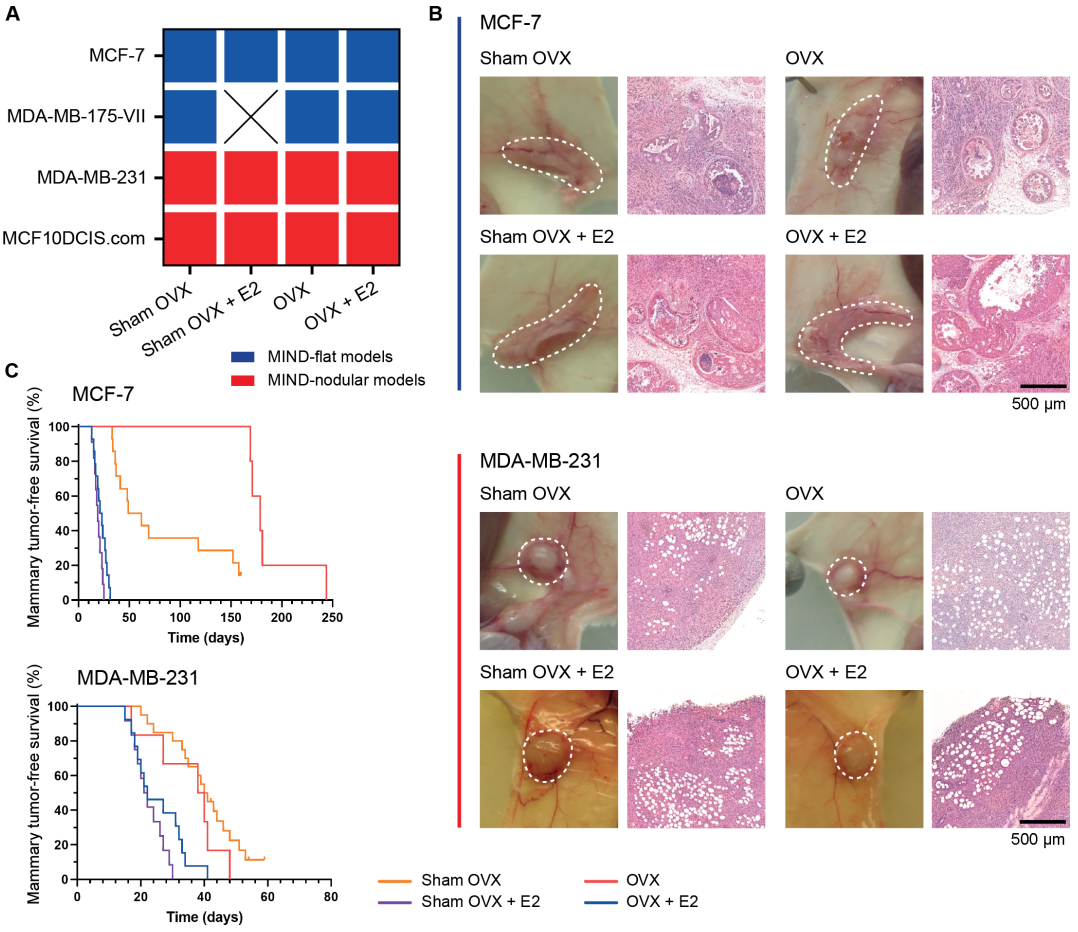

Figure 5: Oestrogen influences growth kinetics but not morphology of MIND-CDX tumours

A) MIND-CDX models of ER$^+$ cell lines MCF-7 and MDA-MB-175-VII do not show differences in tumour growth morphology when animals are sham-ovariectomised (Sham OVX), ovariectomised (OVX) and therefore oestrogen-depleted, or supplemented with oestrogen (Sham OVX + E2 and OVX + E2). All tumour outgrowths show a flat growth pattern. Graphs show the frequency of growth pattern occurrence (%); MCF-7: n=12 for Sham OVX, n=5 for OVX, n=11 for Sham OVX + E2, and n=14 for OVX + E2; MDA-MB-175-VII: n=4 for Sham OVX, n=0 for OVX, n=4 for Sham OVX + E2, and n=2 for OVX + E2. MDA-MB-175-VII cell line xenografts did not show any tumour growth upon ovariectomy; MDA-MB-231: n=17 for Sham OVX, n=6 for OVX, n=12 for Sham OVX + E2, and n=13 for OVX + E2; MCF10DCIS.com: n=7 for Sham OVX, n=6 for OVX, n=14 for Sham OVX + E2, and n=10 for OVX + E2. **B**) Representative photographs and HE stainings showing no changes in growth pattern morphologies of MIND-flat MCF-7 (upper panel) and MIND-nodular MDA-MB-231 (lower panel) tumours after ovariectomy (OVX) or in non-ovariectomised (Sham OVX) controls, with or without supplementation of oestrogen (E2) (scale bars 500 µm). **C**) Tumour growth kinetics are affected by oestrogen as depicted by the mammary tumour-free survival (%) of MCF-7 (upper panel) and MDA-MB-231 (lower panel) tumours after ovariectomy (OVX) or in non-ovariectomised (Sham OVX) controls, with or without supplementation of oestrogen (E2).

Transcriptome analysis identifies upregulated EMT and TGF-β signalling in nodular MIND-CDX tumours

To unravel the molecular mechanisms that underlie the observed bimodal tumour growth morphology, we performed bulk RNA-sequencing analysis on MIND-CDX tumours from the 20 proficiently engrafted cell lines as well as FPT-CDX tumours from 10 cell lines, including all of the corresponding *in vitro* cultured cells (see Supplementary Table 1 for successfully transplanted MIND-CDX tumours included in this analysis).

Unsupervised clustering based on gene expression similarities revealed co-clustering of the *in vitro* cultured cell lines with the corresponding MIND-CDX and FPT-CDX tumours (**Figure 6A**). This indicates that the gene expression profiles mostly reflect tumour-cell intrinsic features that are maintained throughout *in vitro* culturing and *in vivo* tumour development. Additionally, cell lines and tumours clustered together according to IHC subtype (HR^+, $HER2^+$, TN), except for the HR^+ CAMA-1 tumours and the triple-negative MDA-MB-468 and SK-BR-7 tumours, which all clustered within the $HER2^+$ subtype (**Figure 6A**). Intriguingly, the unsupervised clustering resulted in a clear separation between cell lines/tumours that grew either flat or nodular in MIND-CDX models (**Figure 6A**). Here the only exceptions were MIND-nodular SK-BR-7 and MIND-flat SUM149PT CDX tumours, clustering with the samples of the opposite growth pattern in MIND. Furthermore, all MIND-nodular CDX tumours correlated to the basal subtype. Of note, the triple-negative nature of SUM149PT likely confounds the clustering towards other triple-negative tumours and cell lines, which underlines previous indications that molecular subtype does not determine the growth morphology. These data suggest that specific molecular traits correspond with the two observed tumour phenotypes, which remains consistent across multiple BC cell lines.

Following this observation, we aimed to better understand the distinct bimodal growth pattern formation. Differential analysis revealed major differences; however, no clear pathway was recognizable (**Supplementary Figure 10A**). To pinpoint which biological processes could define each growth morphology, we performed gene set variation analysis (GSVA) [13]. Similarly to the unsupervised clustering, flat versus nodular growth in the MIND-CDX models defined the main observed differences in hallmark gene sets (**Figure 6B**). Interestingly, when directly comparing nodular to flat MIND-CDX tumours, FPT tumours, and cell lines, a strong upregulation in hallmarks related to epithelial-to-mesenchymal transition (EMT) and TGF-β pathways

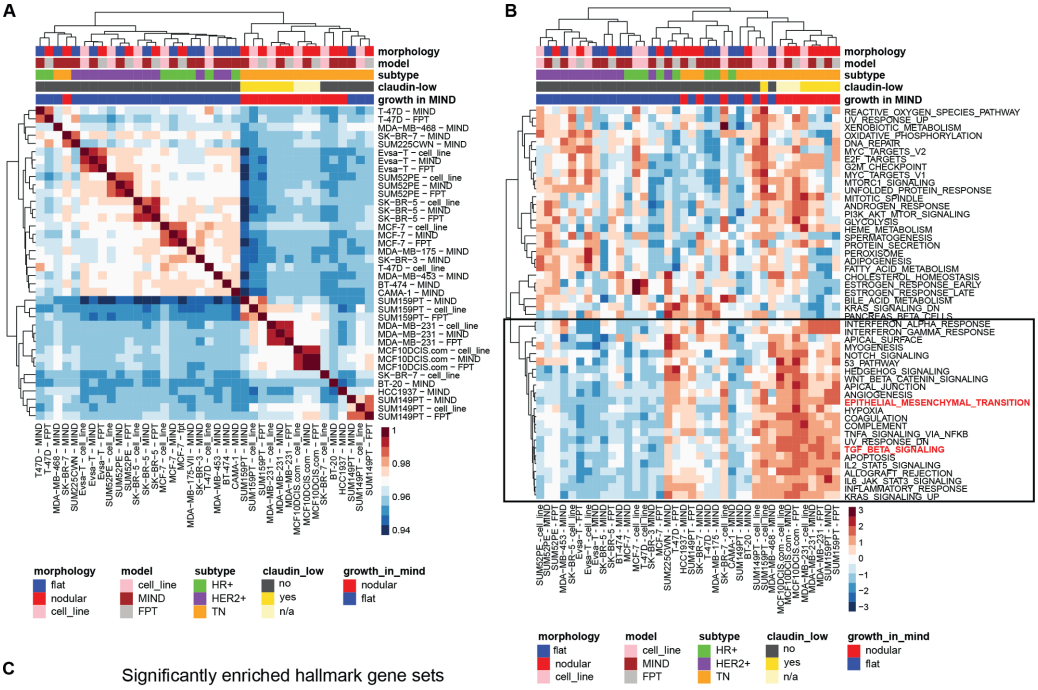
A
morphology
model
subtype
claudin-low
growth in MIND
T-47D – MIND
T-47D – FPT
MDA-MB-468 – MIND
SK-BR-7 – MIND
SUM225CWN – MIND
Evsa-T – cell_line
Evsa-T – MIND
Evsa-T – FPT
SUM52PE – cell_line
SUM52PE – MIND
SUM52PE – FPT
SK-BR-5 – cell_line
SK-BR-5 – MIND
SK-BR-5 – FPT
MCF-7 – cell_line
MCF-7 – MIND
MCF-7 – FPT
MDA-MB-175 – MIND
SK-BR-3 – MIND
T-47D – cell_line
MDA-MB-453 – MIND
BT-474 – MIND
CAMA-1 – MIND
SUM159PT – MIND
SUM159PT – cell_line
SUM159PT – FPT
MDA-MB-231 – cell_line
MDA-MB-231 – MIND
MDA-MB-231 – FPT
MCF10DCIS.com – cell_line
MCF10DCIS.com – MIND
MCF10DCIS.com – FPT
SK-BR-7 – cell_line
BT-20 – MIND
HCC1937 – MIND
SUM149PT – MIND
SUM149PT – cell_line
SUM149PT – FPT
1
0.98
0.96
0.94
morphology
flat
nodular
cell_line
model
cell_line
MIND
FPT
subtype
HR+
HER2+
TN
claudin_low
no
yes
n/a
growth_in_mind
nodular
flat
B
morphology
model
subtype
claudin-low
growth in MIND
REACTIVE_OXYGEN_SPECIES_PATHWAY
UV_RESPONSE_UP
XENOBIOTIC_METABOLISM
OXIDATIVE_PHOSPHORYLATION
DNA_REPAIR
MYC_TARGETS_V2
E2F_TARGETS
G2M_CHECKPOINT
MYC_TARGETS_V1
MTORC1_SIGNALING
UNFOLDED_PROTEIN_RESPONSE
MITOTIC_SPINDLE
ANDROGEN_RESPONSE
PI3K_AKT_MTOR_SIGNALING
GLYCOLYSIS
HEME_METABOLISM
SPERMATOGENESIS
PROTEIN_SECRETION
PEROXISOME
ADIPOGENESIS
FATTY_ACID_METABOLISM
CHOLESTEROL_HOMEOSTASIS
ESTROGEN_RESPONSE_EARLY
ESTROGEN_RESPONSE_LATE
BILE_ACID_METABOLISM
KRAS_SIGNALING_DN
PANCREAS_BETA_CELLS
INTERFERON_ALPHA_RESPONSE
INTERFERON_GAMMA_RESPONSE
APICAL_SURFACE
MYOGENESIS
NOTCH_SIGNALING
P53_PATHWAY
HEDGEHOG_SIGNALING
WNT_BETA_CATENIN_SIGNALING
APICAL_JUNCTION
ANGIOGENESIS
EPITHELIAL_MESENCHYMAL_TRANSITION
HYPOXIA
COAGULATION
COMPLEMENT
TNFA_SIGNALING_VIA_NFKB
UV_RESPONSE_DN
TGF_BETA_SIGNALING
APOPTOSIS
IL2_STAT5_SIGNALING
ALLOGRAFT_REJECTION
IL6_JAK_STAT3_SIGNALING
INFLAMMATORY_RESPONSE
KRAS_SIGNALING_UP
3
2
1
0
−1
−2
−3
morphology
flat
nodular
cell_line
model
cell_line
MIND
FPT
subtype
HR+
HER2+
TN
claudin_low
no
yes
n/a
growth_in_mind
nodular
flat

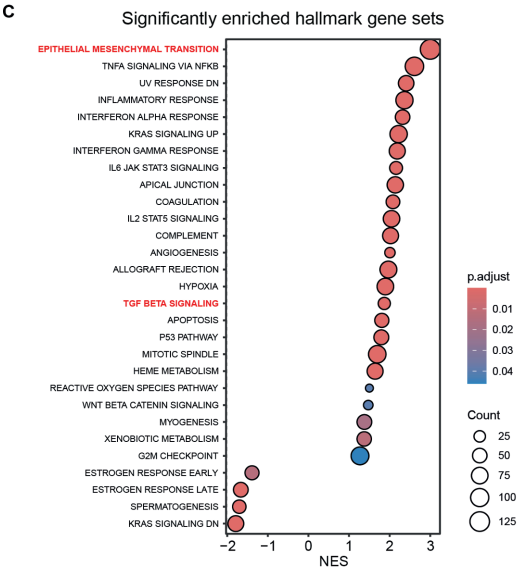
C
Significantly enriched hallmark gene sets
EPITHELIAL MESENCHYMAL TRANSITION
TNFA SIGNALING VIA NFKB
UV RESPONSE DN
INFLAMMATORY RESPONSE
INTERFERON ALPHA RESPONSE
KRAS SIGNALING UP
INTERFERON GAMMA RESPONSE
IL6 JAK STAT3 SIGNALING
APICAL JUNCTION
COAGULATION
IL2 STAT5 SIGNALING
COMPLEMENT
ANGIOGENESIS
ALLOGRAFT REJECTION
HYPOXIA
TGF BETA SIGNALING
APOPTOSIS
P53 PATHWAY
MITOTIC SPINDLE
HEME METABOLISM
REACTIVE OXYGEN SPECIES PATHWAY
WNT BETA CATENIN SIGNALING
MYOGENESIS
XENOBIOTIC METABOLISM
G2M CHECKPOINT
ESTROGEN RESPONSE EARLY
ESTROGEN RESPONSE LATE
SPERMATOGENESIS
KRAS SIGNALING DN
−2
−1
0
1
2
3
NES
p.adjust
0.01
0.02
0.03
0.04
Count
25
50
75
100
125

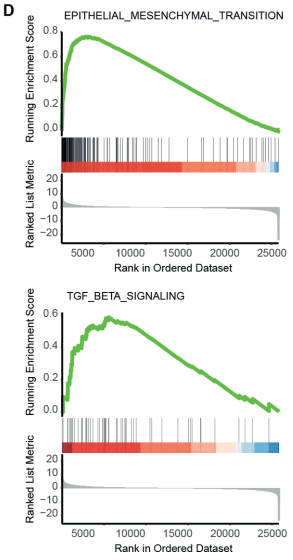
D
EPITHELIAL_MESENCHYMAL_TRANSITION
Running Enrichment Score
0.8
0.6
0.4
0.2
0.0
Ranked List Metric
20
10
0
−10
−20
5000
10000
15000
20000
25000
Rank in Ordered Dataset
TGF_BETA_SIGNALING
Running Enrichment Score
0.6
0.4
0.2
0.0
Ranked List Metric
20
10
0
−10
−20
5000
10000
15000
20000
25000
Rank in Ordered Dataset

Figure 6: Transcriptomic analysis identifies upregulated EMT and TGF-β signalling in nodular MIND-CDX tumours

A) Pearson Correlation heat map for gene expression profiles across different models illustrating the similarity of the samples, with each sample representing a cell line with model attributes presented above the heat map. The top of the heat map displays annotations for each sample, colour-coded based on their attributes for morphology, model, subtype, claudin-low subtype, and growth in MIND-CDX. The claudin-low subtype was identified as previously described [14]. The hierarchical clustering on both the x and y axes groups samples based on their similarity in expression patterns. Colour indications: morphology: flat (blue), nodular (red), cell line (pink); model: cell line (pink), MIND-CDX (brown), FPT-CDX (grey); subtype: HR^+ (green), TN (orange), HER2 (purple); claudin-low subtype: no (dark grey), yes (yellow); growth in MIND-CDX: nodular (red), flat (blue). Scale below the figure depicts Pearson's R score values. **B**) Visualisation of GSVA scores across different samples. Each row of the heat map represents a hallmark pathway, while each column corresponds to a sample. The colour scale indicates the GSVA score, where deep blue marks lower activity and deep red signifies higher activity of the pathway in the respective sample. The annotations on the right of the heat map offer a quick glance into the attributes of each sample, such as morphology, model, subtype, claudin-low subtype, and growth in MIND-CDX. The claudin-low subtype was identified as previously described [14]. EMT and TGF-β pathways are highlighted in red. The hierarchical clustering is based on correlation, categorizing both samples and pathways based on their activity patterns. Colour indications: morphology: flat (blue), nodular (red), cell line (pink); model: cell line (pink), MIND-CDX (brown), FPT-CDX (grey); subtype: HR^+ (green), TN (orange), HER2 (purple); claudin-low subtype: no (dark grey), yes (yellow); growth in MIND-CDX: nodular (red), flat (blue). Scale below the figure depicts normalized (z-score) GSEA score values. **C**) Dot plot displaying the results of gene set enrichment analysis (GSEA) for significantly enriched hallmark gene sets in MIND-nodular tumours. The y-axis lists biological pathways (HALLMARK gene set), the x-axis shows the Normalized Enrichment Score (NES). Dot size represents the adjusted p-value and dot colour indicates the p-value. **D**) Epithelial to mesenchymal transition (gene-set systemic name: M5930), and TGF-β signalling (gene-set systemic name: M5896) GSEA enrichment profiles based on RNA sequencing data comparison for MIND-nodular and MIND-flat tumours.

was apparent (**Figure 6B**, black box and **Supplementary Figure 10B and 11A-B**). In line with this, the MIND-nodular models showed low expression of claudins (i.e. *CLDN3*, *CLDN4*, *CLDN7*), alongside high expression of the genes associated with the claudin-low molecular subtype (**Figure 6A-B and Supplementary Figure 10C**; 9-cell line claudin-low predictor) [14]. Additionally, the MIND-nodular tumours were enriched for hallmarks/pathways related to other potential environmental cues, such as angiogenesis. However, staining of FPT and MIND tumours from all 10 models with CD31, a marker for blood vessels, showed no difference between MIND tumours derived from MIND-nodular and MIND-flat cell lines, ruling out angiogenesis as a driver of the bimodal growth morphology (**Supplementary Figure 12A-E**).

Next, we aimed to address the top differential hallmark resulting from the GSEA analysis, the EMT hallmark, between the nodular and flat phenotype (**Figure 6C and Supplementary Figure 11A+D**). EMT is known to be driven,

at least in part, by the TGF-β signalling pathway [15]. This is in line with our results, showing co-enrichment of EMT with the TGF-β-related hallmark, of which most individual genes were strongly upregulated in nodular versus flat tumours (**Figure 6B-D and Supplementary Figure 11A-B**).

To exclude a potential cell line bias driven by molecular subtype, we separated only TN tumours based on MIND-flat and MIND-nodular growth (2 MIND-flat vs 6 MIND-nodular TN tumours), again revealing upregulation of both EMT and TGF-β in MIND-nodular compared to MIND-flat tumours (**Supplementary Figure 11D**, purple line), although this effect might (in part) be due to the fact that SUM149PT cells originate from inflammatory BC.

Altogether, RNA-sequencing analysis revealed that MIND-nodular and MIND-flat CDX tumours are highly distinct on a molecular level. Despite the major differences between BC cell lines, our analysis allowed us to determine similarities within a heterogeneous population of tumours. Indeed, EMT and TGF-β signalling were the strongest candidates for determining flat or nodular growth morphology across cell lines.

Nodular growth is associated with both autocrine and paracrine TGF-β signalling

To investigate how tumour growth morphology is affected by the transplantation site, we performed GSEA amongst the 6 MIND-flat models and compared their FPT and MIND tumour outgrowths. Unsupervised clustering showed a clear distinction between transplantation site, with EMT and TGF-β hallmark pathway genes enriched in the FPT tumours (**Supplementary Figure 11C and 11D**, green line). This suggests that the nodular growth of MIND-flat models in the mammary FP may be driven by paracrine EMT/TGF-β signalling from the tumour microenvironment. To strengthen this hypothesis, we performed several additional GSEAs (**Supplementary Figure 11D**). FPT tumours from MIND-nodular models showed additional upregulation of EMT/TGF-β compared to their MIND counterparts, providing further support for microenvironmental paracrine signalling (**Supplementary Figure 11D**, blue line). Comparing FPT tumours from MIND-flat vs MIND-nodular models also confirmed an upregulation of EMT and TGF-β genes in the latter, highlighting that autocrine signalling could be inherently present in nodular tumours and enhanced by paracrine microenvironmental cues (**Supplementary Figure 11D**, red line).

This hypothesis was further probed by analysing the tumour microenvironment of both FPT and MIND tumours. As our RNA sequencing data contains reads of both human origin (tumour cells) and mouse origin (innate immune cells and stromal cells), the residual sequencing reads were mapped against the mouse reference genome (GRCm38 (*mm10*)). Following read normalization, mMCP-counter [16] was deployed to estimate the immune and stromal cell composition of the tumour microenvironment (**Figure 7A**). This analysis revealed that, as expected, most immune cells are lacking in these immune-deficient mice. Interestingly, the microenvironment of FPT tumours was characterised by a higher abundance of cancer-associated fibroblasts (CAFs) (**Figure 7B-C**), which showed elevated activation states as assessed by staining against fibroblast activation protein (FAP) (**Figure 7D-E**). FAP-positive CAFs have previously been associated with TGF-β signalling [17,18] and may thus contribute to the paracrine signalling that drives nodular growth of MIND-flat cell lines in the mammary FP.

Together, our extensive transcriptomics analyses indicate that both cell-intrinsic autocrine EMT/TGF-β signalling and paracrine signalling from the FP microenvironment may drive the nodular and aggressive growth phenotype.

TGF-β signalling determines growth kinetics and morphology of MIND-CDX tumours

TGF-β signalling has been shown to be a major regulator of EMT in BC [19,20]. Given the results from our RNA-seq analysis, we aimed to test whether EMT signalling is causally involved in determining tumour growth phenotype and aggressiveness. Therefore, we decided to interfere with TGF-β signalling by perturbing SMAD4, one of the most essential intracellular mediators of downstream transcriptional response of the ligand-activated TGF-β receptor [21,22]. We used CRISPR/Cas9 to genetically inactivate SMAD4 in 7 cell lines that grew either flat (4) or nodular (3) in our MIND-CDX models. After confirming SMAD4 knockout (SMAD4-KO) by western blot (**Supplementary Figure 13A**), we transplanted these cells into NSG mice using the MIND method and included animals transplanted with cells transduced with a non-targeting single-guide (sg)RNA (SMAD4-NT) as a control. Strikingly, SMAD4 inactivation led to a near-complete reversal of the growth pattern of cell lines that initially grew nodular (**Figure 8A-B**). On the other hand, MIND-flat models did not switch their phenotype upon SMAD4 inactivation (**Supplementary**

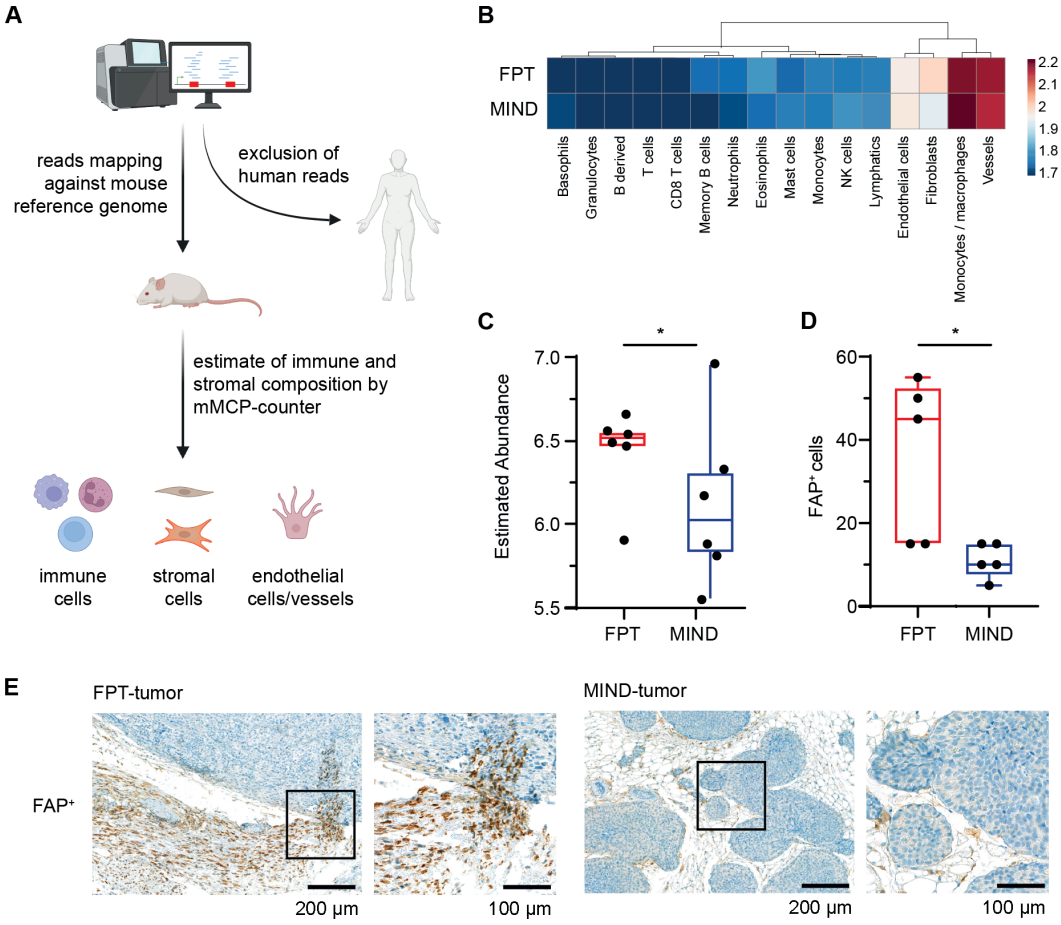

Figure 7: The microenvironment of FPT-CDX tumours is enriched in FAP⁺ CAFs

A) Schematic of workflow used to analyses the microenvironment of CDX using mouse reads in RNA-seq data. **B**) Heat map depicting scaled immune and stromal estimates calculated by mMCP-counter across samples, with hierarchical clustering applied to columns. FPT- and MIND-tumours from the 6 MIND-flat models (Evsa-T, SUM52PE, SUM149PT, SK-BR-5, T-47D, and MCF-7) are compared. **C**) Box plot showing estimated abundance of fibroblasts in FPT tumours compared to MIND tumours from 6 MIND-flat cell lines (p=0.027; Mood's Median Non-parametric test). **D**) Percentage of FAP⁺-stained cells in FPT tumours compared to MIND tumours from 6 MIND-flat cell lines. Tumour and area of 0.5 mm around the tumour borders was assessed. The SUM52PE model was excluded from the analysis as not enough surrounding environment was captured on the FFPE slides (p=0.023; Unpaired t-test). **E**) Representative IHC stainings of FAP expression in the microenvironment of an FPT tumour and a MIND tumour from MIND-flat cell line (T-47D) (scale bar 200 µm, zoom 100 µm).

Figure 13B-C). Of note, SMAD4 knockout did not change the BC molecular subtype, showing that the discovered bimodal growth pattern is regulated by TGF-β and EMT signalling unrelated to HR expression (**Supplementary Figure 14A-B**). Interestingly, SMAD4 inactivation in the initially MIND-nodular models resulted in faster tumour development compared to their SMAD4-NT counterparts (**Supplementary Figure 13D**, upper row). This trend was observed for 50% of the SMAD4-KO cell lines from the MIND-flat group. Here, SUM149PT and Evsa-T SMAD4-KO tumours developed faster, whilst SUM52PE SMAD4-KO cells led to a slightly prolonged tumour latency and MCF-7 SMAD4-KO cells never developed any tumours (**Supplementary Figure 13D**, lower row). Opposingly, by overexpressing a constitutively active TGF-β receptor I (TGFBR1-OE), we aimed to see whether MIND-flat models would revert to a nodular phenotype due to the increased TGF-β signalling (**Supplementary Figure 13E**). Interestingly, the previously strictly MIND-flat tumours now resulted in almost 50% MIND-nodular tumours (**Figure 8C-D**). Similarly to the SMAD4-KOs, TGFBR1-OE did not alter the general morphology of the MIND-nodular models (**Supplementary Figure 13F-G**) and HR and HER2 expression were maintained upon tumour morphology switch (**Supplementary Figure 14C-D**). Interestingly, TGFBR1-OE or SMAD4-KO resulted in relatively similar changes in tumour onset (**Supplementary Figure 13H**).

Collectively, our data confirm a strong causal role of TGF-β signalling in determining the bimodal growth pattern and tumour aggressiveness of BC, regardless of molecular subtype. SMAD4 inactivation in various cell lines reverted initially MIND-nodular tumours to the MIND-flat phenotype, and TGFBR1-OE potentiated the opposite. Thus, this study highlights cell-intrinsic autocrine TGF-β signalling as a key determinant of *in vivo* BC growth morphology and aggressiveness.

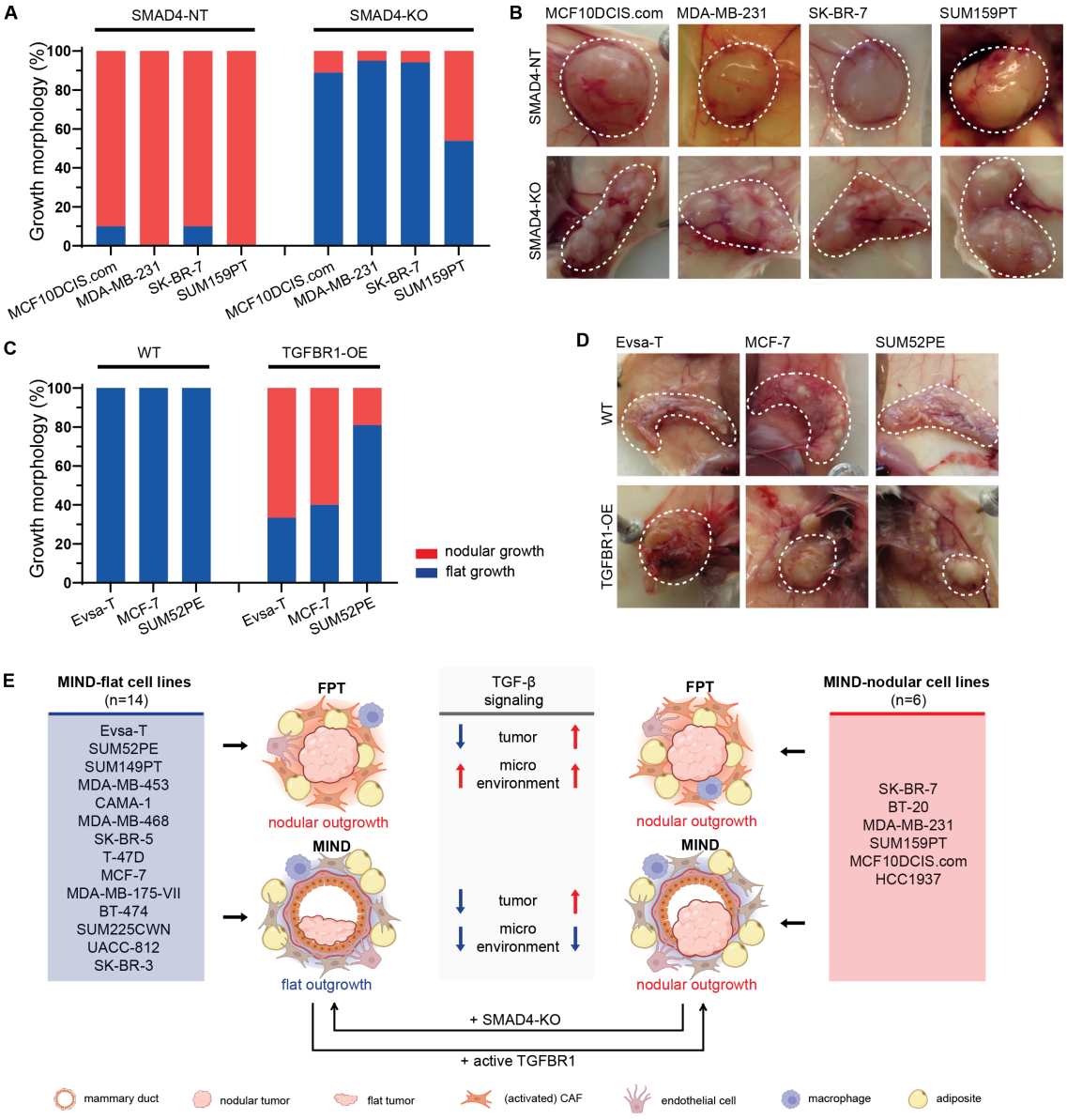
A
SMAD4-NT
SMAD4-KO
Growth morphology (%)
MCF10DCIS.com
MDA-MB-231
SK-BR-7
SUM159PT
B
MCF10DCIS.com
MDA-MB-231
SK-BR-7
SUM159PT
SMAD4-NT
SMAD4-KO
C
WT
TGFBR1-OE
Growth morphology (%)
Evsa-T
MCF-7
SUM52PE
nodular growth
flat growth
D
Evsa-T
MCF-7
SUM52PE
WT
TGFBR1-OE
E
MIND-flat cell lines
(n=14)
Evsa-T
SUM52PE
SUM149PT
MDA-MB-453
CAMA-1
MDA-MB-468
SK-BR-5
T-47D
MCF-7
MDA-MB-175-VII
BT-474
SUM225CWN
UACC-812
SK-BR-3
FPT
nodular outgrowth
MIND
flat outgrowth
TGF-β
signaling
tumor
micro
environment
tumor
micro
environment
FPT
nodular outgrowth
MIND
nodular outgrowth
MIND-nodular cell lines
(n=6)
SK-BR-7
BT-20
MDA-MB-231
SUM159PT
MCF10DCIS.com
HCC1937
+ SMAD4-KO
+ active TGFBR1
mammary duct
nodular tumor
flat tumor
(activated) CAF
endothelial cell
macrophage
adiposite

Figure 8: TGF-β signalling determines growth kinetics and morphology of MIND-CDX tumours

A) SMAD4 inactivation changes the growth pattern of MCF10DCIS.com, MDA-MB-231, SK-BR-7, and SUM159PT MIND-CDX tumours from nodular to flat. Graphs show the frequency of growth pattern occurrence (nodular vs flat, %): SMAD4-NT: MCF10DCIS.com: 90 (n= 9) vs 10 (n=1), MDA-MB-231: 100 (n=11) vs 0 (n=0), SK-BR-7: 90 (n=9) vs 10 (n=1), SUM159PT: 100 (n=9) vs 0 (n=0) and SMAD4-KO: MCF10DCIS.com: 11 (n=2) vs 89 (n=16), MDA-MB-231: 5 (n=1) vs 95 (n=19), SK-BR-7: 6 (n=1) vs 94 (n=16), SUM159PT: 46 (n=6) vs 54 (n=7). **B**) Representative photographs of SMAD4-NT (upper row) and SMAD4-KO (lower row) MIND-CDX tumours from MCF10DCIS.com, MDA-MB-231, SK-BR-7, and SUM159PT cell lines, showing the phenotypic conversion of the nodular growth pattern in SMAD4-NT controls towards flat growth morphology in SMAD4-KO tumours. **C**) TGFBR1-OE changes the growth pattern of Evsa-T, MCF-7, and SUM52PE MIND-CDX tumours from flat to nodular. Graphs show the frequency of growth pattern occurrence (flat vs nodular, %): TGFBR1-WT: Evsa-T: 100 (n= 10) vs 0 (n=0), MCF-7: 100 (n=13) vs 0 (n=0), SUM52PE: 100 (n=17) vs 0 (n=0), and TGFBR1-OE: Evsa-T: 33 (n= 3) vs 67 (n=6), MCF-7: 40 (n=6) vs 60 (n=9), SUM52PE: 81 (n=17) vs 19 (n=4). **D**) Representative photographs of TGFBR1-WT (upper row) and TGFBR1-OE (lower row) MIND-CDX tumours from Evsa-T, MCF-7, and SUM52PE cell lines, showing the phenotypic conversion of the flat growth pattern in TGFBR1-WT controls towards nodular growth morphology in TGFBR1-OE tumours. **E**) Schematic depicting growth morphologies in different environments and with different intrinsic signalling pathway alterations. MIND-nodular models possess autocrine TGF-β signalling and therefore display context-independent aggressive, nodular growth. In contrast, nodular growth of MIND-flat models depends on paracrine TGF-β signalling that may be provided by FAP-positive cancer-associated fibroblasts in the FPT but not the MIND microenvironment. Abrogation of TGF-β signalling by SMAD4-KO inhibits nodular growth of intraductally injected MIND-nodular models (n=4), whereas constitutively active TGF-β signalling via overexpression of TGFBR1 induces nodular growth of intraductally injected MIND-flat models (n=3).

Discussion

To this day, mechanisms that underpin the invasiveness of BC remain poorly understood. To shed light on this question, we harnessed a large panel of CDX models spanning all intrinsic BC subtypes, using FP and intraductal orthotopic transplantation methods (FPT and MIND, respectively). Our study includes a comprehensive characterisation of 20 MIND-CDX models, including tumour latencies and engraftment rates, molecular subtype, gene expression profiles, and (for 10 models) metastatic potential. This is, to our knowledge, the first categorical, large-scale characterisation of orthotopic CDX models based on workhorse cell lines that have been generated and used in BC research for decades. As such, we have established an important resource allowing a better and more rational selection of the most appropriate *in vivo* model(s) to address a specific research question.

Despite its clinical relevance, *in situ* disease has rarely been observed in xenograft studies and studying this stage of disease has been hindered by

the lack of appropriate models. To overcome this limitation, Hutten *et al*., have recently published a large resource of patient-derived MIND models of DCIS [23]. Intriguingly, we also observed DCIS in all MIND-flat CDX models as well as two MIND-nodular models, even though all lines have been derived from IBC or metastatic disease. This may be attributed to the fact that, in contrast to existing literature, this study transplanted a low number of tumour cells, allowing the observation of full evolution of tumour growth from *in situ* to locally invasive BC and ultimately metastatic disease. Notably, while MCF10DCIS.com cells were previously published as a resource for DCIS modelling [24-26], they developed poorly differentiated and HR-negative DCIS lesions after MIND transplantation that rapidly progressed to nodular-growing invasive tumours (median latency of 22.5 days). Altogether, our data emphasize that critical evaluation should be taken into account when choosing an appropriate *in vivo* model for studying DCIS.

The tumour outgrowths from each cell line in this study manifested in one of two ways: (*1*) nodular growth, irrespective of transplantation method or (*2*) flat growth upon intraductal injection and nodular growth upon FPT. RNA-seq analysis of our entire panel of CDX models allowed the identification of molecular commonalities that span across models, eliminating potential cell line and BC subtype biases. Through this, we linked the strictly bimodal growth pattern amongst all primary tumours to TGF-β signalling, which acted independently of the BC subtype. This corroborates with and builds upon a recent study where MIND and FPT transplantation of MCF-7 cells yielded flat and nodular tumours, respectively [11]. However, with our expanded panel of 20 BC cell lines we show that these two growth patterns can also be observed within MIND-CDX models. This work critically underlines how choice of cell line model and transplantation method may significantly impact the results of *in vivo* animal studies.

TGF-β has mostly been implicated as a driver of metastasis. Interestingly, a role for TGF-β in tumour growth morphology in metastatic brain cancer was recently identified, where two distinct growth patterns were observed, namely perivascular and spheroidal [27]. However, whilst TGF-β is widely studied in the metastatic setting, its effects on primary tumour growth is underexplored. We find TGF-β at the center of determining primary BC growth morphology. Mechanistically, in line with the notion that TGF-β signalling is a potent driver of EMT [22,28], we show that CRISPR/Cas9-mediated knockout of its main regulator, SMAD4 [22], causes a striking near-complete conversion of

aggressive, MIND-nodular CDX tumours into MIND-flat lesions. Conversely, overexpression of a constitutively active TGFBR1 partially reverted MIND-flat tumours to the MIND-nodular growth pattern. Interestingly, despite their flat growth morphology, the SMAD4-KO tumours grew faster than the SMAD-NT control tumours. This is in line with existing literature, which postulates a dual role for TGF-β [28,29], where its signalling impairs tumourigenesis but promotes pulmonary metastasis in MMTV-Neu transgenic mice [29]. We provide evidence for the latter as well, showing that MIND-nodular CDX tumours with TGF-β upregulation harbour a higher potential to metastasize to different organs than MIND-flat tumours. Additionally, our in-depth analysis of metastatic potential from 10 different MIND-CDX models highlights SK-BR-7 as an excellent preclinical *in vivo* model of BC metastasis formation. This cell line metastasizes to multiple organs with high efficiency and in a very reproducible manner.

We find TGF-β and EMT at the centre of determining primary BC growth pattern, independent of molecular subtype. Cell lines harbouring cell-intrinsic autocrine TGF-β and EMT signalling grow nodular despite their environment (**Figure 8E**, right), whereas cell lines relying on paracrine signalling from the microenvironment, specifically from CAFs known to produce TGF-β ligands, grow flat in the mammary duct and nodular in the FP (**Figure 8E**, left). Perturbing cell-intrinsic TGF-β signalling in either direction reverses the growth pattern. Therefore, our data suggests that the ability of the microenvironment to affect BC tumour growth pattern relies strictly on tumour cell-intrinsic molecular features. However, although we discover TGF-β as the key regulator of the bimodal tumour growth pattern, many studies have unveiled significant crosstalk between the TGF-β pathway and other major signalling cascades. JAK-STAT, the PI3K-Akt and NFκB pathways, among others, have been shown to affect TGF-β signalling [30]. Additionally, nuclear hormone receptors, such as ER and GR, tend to have a downregulatory function on TGF-β signalling, potentially underlying subtype-related correlations we observe in this study [31,32]. Having unveiled TGF-β as a key regulator of primary BC growth pattern and aggressiveness, the aforementioned crosstalk may be of additional relevance in determining tumour growth outcomes and should be subject of further investigation.

In sum, by generating and comprehensively characterising a large panel of BC xenograft models, we provide a detailed resource enabling improved decision making when selecting fitting models. Furthermore, we uncover meaningful

insights into BC growth morphology and identify TGF-β as a key orchestrator of primary tumour growth morphology and aggressiveness. These findings deepen our understanding of BC biology and may inform the development of novel therapeutic strategies aimed at modulating tumour aggressiveness and mitigating metastatic progression.

Materials and Methods

Cell culturing

Human BC cell lines were cultured in respective medium according to Supplementary Table 1. To stably express luciferase, all cells were transduced with pLenti CMV Puro LUC (w168-1) (addgene 17477, RRID:Addgene_17477) [33] using lentiviral supernatants of the same IU/ml in the presence of 8 µg/ml polybrene. 24 hours after transduction, puromycin selection was performed using 0.5-2 µg/ml puromycin (Thermo Fisher Scientific, A11138) until selection was complete. Transduction was tested via bioluminescence assays using 3.75 mg/ml beetle luciferin (Promega). All cell lines were cultured in standard incubators at 37°C and with 5% CO_2. Routine mycoplasma tests were performed using the MycoAlert Mycoplasma Detection Kit (Lonza, LT07-218). Before xenografting, cells underwent thorough PCR testing for the following mouse pathogens: Corynebacterium bovis, Corynebacterium sp. (HAC2), Ectromelia, EDIM, Hantaan, K virus, LCMV, LDEV, MAV1, MAV2, mCMV, MHV, MNV, Mouse kidney parvovirus (MKPV), MPV, MTV, MVM, Mycoplasma pulmonis, Mycoplasma sp., Parvovirus, Polyoma, PVM, REO3, Sendai, and TMEV (performed by Idexx). In addition, 10 cell lines (SUM52PE, MCF-7, T-47D, Evsa-T, SK-BR-5, SUM149PT, MCF10DCIS.com, MDA-MB-231, SK-BR-7, SUM159PT) underwent cell line authentication (performed by Eurofins, the Netherlands). Detailed information including RRIDs for all cell lines are listed in Supplementary Table 1.

Immunofluorescence of cell lines

1000 cells were seeded onto glass coverslips in a 24-well plate and cultured for 24h in their respective media (see Supplementary Table 1). Cells were fixed for 15 min with ice-cold 4% paraformaldehyde in PBS, permeabilised for 10 min with 0.5% Triton-X-100/PBS, blocked with 5% bovine serum albumin (BSA)/5% goat serum in PBS for 30 min, followed by primary antibody incubation in 1% BSA/PBS overnight at 4°C. Secondary antibody incubation was performed for 1 h at room temperature. DAPI was used to stain the nuclei.

Immunofluorescence images were taken at a confocal microscope (SP8, Leica Mannheim). Antibodies are listed in Supplementary Table 2.

Generation of TGF-β pathway modified cell lines

Cell lines with CRISPR-Cas9 mediated SMAD4-KO: Human BC cell lines were cultured as described above and in Supplementary Table 1. For gene-editing of the cell lines, lentiviral sgRNA vectors were generated using lentiCRISPRv2 (addgene, 52961, RRID: Addgene_52961). The guide RNA sequences used were GGATACGTGGACCCTTCTGG for SMAD4 knockout and TGATTGGGGGTCGTTCGCCA as a non-targeting control. Cells were transduced with the lentiCRISPRv2 plasmid at 70-80% confluence using 8 µg/µl polybrene. 24 hours post transduction the cell medium was refreshed with the respective growth medium containing 2 µg/ml puromycin and selected for an additional 72 hours. Successful editing of the cells was confirmed by Sanger sequencing and consecutive TIDE analysis using the following primers: TCCATCTCCCCTCCCTTTACC (FOR) and CACCGACAATTAAGATGGAGTGCT (REV). In addition, loss of the targeted protein was assessed by immunoblotting.

Cell lines with constitutively active TGFBR1 overexpression: Human BC cell lines were cultured as described above and in Supplementary Table 1. For constitutively active expression of the TGFBR1, the cDNA was cloned out of a pCW57.1 lentiviral vector (addgene, 41393, RRID: Addgene_41393) with inducible TGFBR1 expression which was a kind gift from Peter ten Dijke and lifted over into a pLex305 lentiviral vector (addgene, 41390, RRID: Addgene_41390). Cells were transduced and selected as described above.

RNA isolation and RT-qPCR

WT and TGFBR1-OE cells were pelleted and lysed in TRIzol. Total RNA extraction was performed using chloroform/isopropanol. Pellets were washed with ethanol, air dried, and resuspended in nuclease-free H_2O. Purified RNA was quantified using the DS-11 Series Spectrophotometer/Fluorometer (DeNovix) and subjected to reverse transcriptase reaction using random hexamer primers, 10x RT buffer, 25mM MgCl2, 0.1M DTT, RNAse OUT, and SuperScript III reverse transcriptase (Invitrogen, 18080093). qPCR was performed using the SensiFAST SYBR Hi-Rox Kit (BIO-92005, Bioline) and the QuantStudio 5 Real-Time PCR System (Thermo Fisher Scientific, A34322) operated with the QuantStudio Real-Time PCR Software (Thermo Fisher Scientific, version 1.7.2). Primer-BLAST [34] was used to design primers with the following

sequences for TGFBR1: 5'-GACCTCTCTCCCCAGATGGAGGCGGCGG-3' (FOR) and 5'-ATCCAGAGGTTGATTCATTTTGATGCCTTCCTGTTGACTG-3' (REV) and USF1: 5'-ATGGAGAGCACCAAGTCTGG-3' (FOR) and 5'-TGGTTACTCTGCCGAAGCTC-3' (REV). Relative quantified cDNA was normalized using *USF1* as the housekeeping transcript.

Mouse models

Mammary fat-pad transplantation (FPT) models: For the generation of FPT-CDX models, cell lines were transplanted into mouse mammary FPs as described [35]. 100,000 suspended single cells in PBS were transplanted in the FP of the fourth mammary glands of 8-week-old female NOD-Scid IL2Rg^{null} (NSG) mice by making a small incision, releasing the cells into the FP with a 34G needle and suturing the cut with one stitch.

Mammary intraductal (MIND) injection models: To establish MIND-CDX models, human BC cell lines were intraductally injected as previously described [36]. Cells were dissociated with trypsin (0.05 or 0.25%) and 25,000 cells in PBS per mammary gland were injected into the third and/or forth glands of 8-week-old female NSG mice (RRID: IMSR_JAX:005557) by using a 34G needle.

Mastectomy: Mice were intraductally injected in a fourth mammary gland with human BC cells as described above. Mastectomy was performed when the primary tumour reached a size of 500 mm^3. Analgesia was provided using temgesic and rimadyl pre-and post-surgery according to the institute's standard. All mice were monitored via *in vivo* bioluminescence imaging for metastatic disease.

Oestrogen supplementation: 17β-oestradiol (Innovative Research of America) was supplemented in form of a 90-day release pellet with 0.18 mg/pellet, subcutaneously implanted into the neck of 8-week-old female NSG mice 7 days prior to tumour inoculation via intraductal injection. Pellets were replaced every 90 days.

Sham ovariectomy & ovariectomy: Sham ovariectomy or ovariectomy was performed 7 days prior to tumour inoculation via intraductal injection as described above. Two small incisions were made, to ensure the (mock) removal of both ovaries. Analgesia was given according to the institute's standard.

General guidelines: The xenograft model cohorts were monitored twice weekly and mammary tumour-free survival was scored for each injected or transplanted mammary gland individually when palpable tumours were detected. The engraftment rate was calculated on the basis of these events. In addition, all animals were monitored via *in vivo* bioluminescence imaging (IVIS) on a weekly basis. Mammary tumour-specific survival was scored when the cumulative mammary tumour burden reached a volume of 1,500 mm^3. The maximal permitted disease endpoints were not exceeded at any point within this study. Mice sacrificed for other reasons were censored and excluded for further analysis. At sacrifice, mammary glands were collected in formalin and analysed for histopathological abnormalities. Tumour measurements and post-mortem analysis were performed in blinded fashion. The mouse colonies were housed in a certified animal facility with a 12-hour light/dark cycle in temperature-controlled rooms. Mice were kept in individually ventilated cages and food and water were provided ad libitum. All animal experiments were approved by the Animal Ethics Committee of the Netherlands Cancer Institute and performed in accordance with institutional, national, and European guidelines for Animal Care and Use.

In vivo bioluminescence imaging

Prior to engraftment all cell lines were engineered to hold a luciferase carrying cassette with inducible expression via luciferin injection (addgene, 17477, RRID: Addgene_17477) [33]. *In vivo* bioluminescence imaging was performed weekly by intraperitoneal injection of 150 mg/kg beetle luciferin (Promega) as previously described [37]. Signal intensity was measured in a size-fixed square and total radiance was quantified (total flux was measured in p/sec/cm^2/sr; photons per second per cm^2 per steradian).

Histology and immunohistopathology

Upon mouse sacrifice tissues were formalin-fixed and paraffin-embedded. Haematoxylin and eosin (H&E) as well as immunohistochemical stainings (IHC) were performed using routine procedures. For IHC stainings, antigen retrieval was performed with Tris/EDTA (pH 9.0) (Tris: Sigma, 252859; EDTA: Sigma, EDS) for ER-α, HER2, Ki67, Casp-3, CD31 or citrate buffer (pH 6.0) (Scytek, CBB999) for PR.

Sections were incubated with primary antibodies (Supplementary Table 2) overnight at 4°C. EnVision+ HRP Labelled Polymer Anti-Rabbit System (Dako, K4003) was used for labelling and Liquid DAB+ Substrate Chromogen System

(Dako, K3468) for visualisation of primary antibodies and counterstain with haematoxylin was performed.

Immunohistochemistry for FAP-a: Immunohistochemistry of the FFPE tumour samples was performed on a Discovery Ultra autostainer (Ventana Medical Systems). Briefly, paraffin sections were cut at 3 µm, heated at 75°C for 28 minutes and deparaffinised in the instrument with EZ prep solution (Ventana Medical Systems). Heat-induced antigen retrieval was carried out using Cell Conditioning 1 (CC1, Ventana Medical Systems) for 64 minutes at 95°C. FAP-a was detected using clone EPR20021 (1/100 dilution, 64 minutes at 37°C, Abcam). Bound antibody was detected using the anti-Rb HQ for 12 minutes at 37°C, followed by Anti-HQ HRP for 12 minutes at 37°C, after which the ChromoMap DAB Kit (Ventana Medical Systems) was applied. Slides were counterstained with Hematoxylin and Bluing Reagent (Ventana Medical Systems). The SUM52PE model was excluded from the analysis as not enough surrounding environment was captured on the FFPE slides.

Digitalization and analysis: H&E slides were used for diagnosis and classification of mammary tumours according to the international consensus of mammary pathology [38]. IHC stains were quantitatively analysed by evaluating positivity according to clinical standards. All slides were reviewed and quantified by two trained pathologists (X.C. and J-Y. S.) in blinded fashion. Slides were digitally processed using a PANNORAMIC 1000 whole slide scanner (3DHISTECH) and captured with the Slidescore software (www.slidescore.com). QuPath software (v.0.4.4) was used for image analysis and quantification of positively stained cells.

RNA-sequencing of human cancer cell lines

RNA-sequencing of cultured cells was performed as previously described [39]. In short, 10^6 cells were lysed in RLT Lysis Buffer (Qiagen, 79216) containing 1% 2-mercaptoethanol. Total RNA was then extracted using the RNeasy Mini Kit (Qiagen, 74104) according to the manufacturer's instructions. Quality and quantity of the extracted RNA was assessed using the Nanodrop and 2100 Bioanalyser RNA Nano Chip systems. RNA samples with RIN>8 were subjected to polyA-stranded library preparation using the TruSeq RNA Library Prep Kit v2 (Illumina, RS-122-2001/2) according to the manufacturer's guidelines and the quality was re-assessed using the 2100 Bioanalyser. The library prepared RNA was pooled into a 10 nM sequencing stock solution and libraries were sequenced with 65 bp single reads using the HiSeq 2500

System with V4 chemistry. Sequencing reads were mapped to the human reference genome GRCh38 (genecode v32 CTAT) using STAR (version 2.7.2) [40] with the recommended parameters to subsequently run STAR-Fusion [41]. Gene expression read counts were quantified via featureCounts (version 1.6.2) based on gene structures defined in GRCh38.

RNA-sequencing of xenograft tumours

30-35 mg of fresh-frozen tumour pieces were thawed in RLT Lysis Buffer (Qiagen, 79216) containing 1% 2-mercaptoethanol and subsequently subjected to RNA isolation with the RNeasy Mini Kit (Qiagen, 74104) according to the manufacturer's guidelines. Quality and quantity of the extracted RNA was assessed using the Nanodrop and 2100 Bioanalyser RNA Nano Chip systems. RNA samples with RIN>8 were subjected to polyA-stranded library preparation and sequenced and mapped as described for human BC cells.

Analysis of RNA-sequencing data from cell lines and xenografted tumours

General RNA Sequencing Analysis: To assess the similarities between different samples, a Pearson correlation analysis was conducted. Specifically, the assay function from the DESeq2 package (version 1.42.0, RRID:SCR_000154) was used to extract the regularized log-transformed counts from the vsd object. A matrix of Pearson correlation coefficients was then generated using the cor function (stats package; version 4.3.2) in R. Differential gene expressions were performed using R package DESeq2 (version 1.42.0) using the standard approach.

Distinct colours were assigned to the annotations, representing model (three models: cell line, MIND-CDX, and FPT-CDX), morphology (three forms: flat, nodular, and cell line), subtype (three types: HR^+, TN, and HER2), claudin-low subtype (two levels: no and yes), and growth in MIND (two levels: nodular and flat). The resulting correlation matrix, complemented with these annotations, was visualized using the pheat map package (version 1.0.12), generating a heat map that reflects the correlations between the samples.

Gene Set Variation Analysis (GSVA): GSVA was employed to assess pathway activities across different samples. The analysis used the normalized and variance stabilized gene expression matrix. The hallmark gene sets from the Molecular Signatures Database (MSigDB) were employed for the analysis. GSVA scores were calculated using the gsva method (gsva package; version

1.50.0). Annotations representing model (consisting of three models: cell line, MIND-CDX, and FPT-CDX), morphology (containing three morphologies: flat, nodular, and cell line), subtype (featuring three types: HR^+, TN, and HER2), and growth in MIND (with two levels: nodular and flat) were included to describe the samples. This colour palette represents the range of GSVA scores, with deep blue indicating lower pathway activity and deep red higher pathway activity. Annotations were coloured as previously defined for each attribute.

mMCF-count immune and stromal estimation: To explore the stromal compartment the RNA sequencing reads were aligned to the mouse genome and analysed using the mMCPcounter R package [16] to estimate the abundance of immune and stromal cell populations. The normalized expression matrix was derived from the variance-stabilizing transformation from the DESeq2 package. This matrix was used as input for the mMCPcounter. estimate function, leveraging the predefined gene signatures included in mMCPcounter.

Statistical analysis and reproducibility

RNA sequencing data analysis was performed using R (version 4.3.2). For *in vitro* and *in vivo* experiments Prism (version 9, GraphPad Software, RRID:SCR_002798) was used for visualisation and analysis of the data. Sample sizes for *in vivo* studies were determined using G*Power software (version 3.1, RRID:SCR_013726) [42].

Data availability

All data generated or analysed during this study are deposited in GEO under the accession number GSE263474. The human reference genome (GRCh38 Gencode v32 CTAT) used for RNA-seq data analysis is available in CTAT Genome Lib data resources: https://data.broadinstitute.org/Trinity/CTAT_RESOURCE_LIB. All other raw data generated in this study are available upon request from the corresponding author.

Author Disclosures

The authors have nothing to disclose.

Author contributions

C.L., J.M., J.v.R, S.P. and J.J. conceived the ideas and designed the experiments. C.L., J.M., B.d.K. and A.P.N. performed the laboratory experiments. C.L., B.d.K., M.B., T.E., S.J.H., N.P. and B.S. performed the animal

experiments. C.L., N.P., B.S. and M.v.d.V. supervised the animal experiments. C.L. and J.M. analysed laboratory and animal experimental data. X.C. and J-Y.S. assessed the histopathology and immunohistochemistry of all tumours. S.P. and J.B. performed the bioinformatics analysis. C.L., J.M., B.d.K. and S.P. wrote the manuscript. J.J. acquired the funding for this study.

Acknowledgements

We thank Dr. Daniel Zingg for useful discussions and input on the manuscript. Our gratitude goes to everyone from the Mouse Clinic for Cancer and Aging (MCCA) that helped with the animal work surrounding the TGF-β pathway disruption experiments as well as Milo van Batenburg who was already involved in the work prior to joining the MCCA. All staff at the NKI animal facility, especially the T1 and T3 teams for organization, logistics, and the many NSG mice included in this study. We would like to thank the animal pathology, the genomics core facility and the core facility for molecular pathology and biobanking.

This work was funded by Cancer Research UK and by the Dutch Cancer Society (KWF; ref.C38317/A24043). This work is part of the Oncode Institute, which is partly financed by the Dutch Cancer Society. Research at the Netherlands Cancer Institute is supported by institutional grants from the Dutch Cancer Society and the Dutch Ministry of Health, Welfare and Sport.

References

1 Sung, H. *et al.* Global Cancer Statistics 2020: GLOBOCAN Estimates of Incidence and Mortality Worldwide for 36 Cancers in 185 Countries. *CA Cancer J Clin* **71**, 209-249, doi:10.3322/caac.21660 (2021).

2 Lutz, C., Messal, H. A., Vareslija, D. & Prekovic, S. The complex landscape of luminal breast cancer. *Endocrine-Related Cancer*, ERC-24-0201, doi:10.1530/erc-24-0201 (2024).

3 Nolan, E., Lindeman, G. J. & Visvader, J. E. Deciphering breast cancer: from biology to the clinic. *Cell* **186**, 1708-1728, doi:10.1016/j.cell.2023.01.040 (2023).

4 Lasfargues, E. Y. & Ozzello, L. Cultivation of human breast carcinomas. *J Natl Cancer Inst* **21**, 1131-1147 (1958).

5 Sharma, M. P., Shukla, S. & Misra, G. Recent advances in breast cancer cell line research. *Int J Cancer* **154**, 1683-1693, doi:10.1002/ijc.34849 (2024).

6 Witt, B. L. & Tollefsbol, T. O. Molecular, Cellular, and Technical Aspects of Breast Cancer Cell Lines as a Foundational Tool in Cancer Research. *Life (Basel)* **13**, doi:10.3390/life13122311 (2023).

7 Dai, X., Cheng, H., Bai, Z. & Li, J. Breast Cancer Cell Line Classification and Its Relevance with Breast Tumor Subtyping. *J Cancer* **8**, 3131-3141, doi:10.7150/jca.18457 (2017).

8 Souto, E. P., Dobrolecki, L. E., Villanueva, H., Sikora, A. G. & Lewis, M. T. In Vivo Modeling of Human Breast Cancer Using Cell Line and Patient-Derived Xenografts. *J Mammary Gland Biol Neoplasia* **27**, 211-230, doi:10.1007/s10911-022-09520-y (2022).

9 Deng, N. *et al.* Deep whole genome sequencing identifies recurrent genomic alterations in commonly used breast cancer cell lines and patient-derived xenograft models. *Breast Cancer Res* **24**, 63, doi:10.1186/s13058-022-01540-0 (2022).

10 Riaz, M. *et al.* Growth and metastatic behavior of molecularly well-characterized human breast cancer cell lines in mice. *Breast Cancer Res Treat* **148**, 19-31, doi:10.1007/s10549-014-3142-0 (2014).

11 Sflomos, G. *et al.* A Preclinical Model for ERα-Positive Breast Cancer Points to the Epithelial Microenvironment as Determinant of Luminal Phenotype and Hormone Response. *Cancer Cell* **29**, 407-422, doi:10.1016/j.ccell.2016.02.002 (2016).

12 Rosen, J. M. & Roarty, K. Paracrine signalling in mammary gland development: what can we learn about intratumoral heterogeneity? *Breast Cancer Research* **16**, 202, doi:10.1186/bcr3610 (2014).

13 Hänzelmann, S., Castelo, R. & Guinney, J. GSVA: gene set variation analysis for microarray and RNA-seq data. *BMC Bioinformatics* **14**, 7, doi:10.1186/1471-2105-14-7 (2013).

14 Prat, A. *et al.* Phenotypic and molecular characterization of the claudin-low intrinsic subtype of breast cancer. *Breast Cancer Res* **12**, R68, doi:10.1186/bcr2635 (2010).

15 Dongre, A. & Weinberg, R. A. New insights into the mechanisms of epithelial-mesenchymal transition and implications for cancer. *Nat Rev Mol Cell Biol* **20**, 69-84, doi:10.1038/s41580-018-0080-4 (2019).

16 Petitprez, F. *et al.* The murine Microenvironment Cell Population counter method to estimate abundance of tissue-infiltrating immune and stromal cell populations in murine samples using gene expression. *Genome Medicine* **12**, 86, doi:10.1186/s13073-020-00783-w (2020).

17 Huang, M. *et al.* TGF-β1-activated cancer-associated fibroblasts promote breast cancer invasion, metastasis and epithelial-mesenchymal transition by autophagy or overexpression of FAP-α. *Biochemical Pharmacology* **188**, 114527, doi:https://doi.org/10.1016/j.bcp.2021.114527 (2021).

18 Ping, Q. *et al.* TGF-β1 dominates stromal fibroblast-mediated EMT via the FAP/VCAN axis in bladder cancer cells. *J Transl Med* **21**, 475, doi:10.1186/s12967-023-04303-3 (2023).

19 Muraoka, R. S. *et al.* Increased malignancy of Neu-induced mammary tumors overexpressing active transforming growth factor beta1. *Mol Cell Biol* **23**, 8691-8703, doi:10.1128/mcb.23.23.8691-8703.2003 (2003).

20 Muraoka-Cook, R. S. *et al.* Conditional overexpression of active transforming growth factor beta1 in vivo accelerates metastases of transgenic mammary tumors. *Cancer Res* **64**, 9002-9011, doi:10.1158/0008-5472.Can-04-2111 (2004).

21 Attisano, L. & Wrana, J. L. Signal transduction by the TGF-beta superfamily. *Science* **296**, 1646-1647, doi:10.1126/science.1071809 (2002).

22 Zhao, M., Mishra, L. & Deng, C. X. The role of TGF-β/SMAD4 signalling in cancer. *Int J Biol Sci* **14**, 111-123, doi:10.7150/ijbs.23230 (2018).

23 Hutten, S. J. *et al.* A living biobank of patient-derived ductal carcinoma in situ mouse-intraductal xenografts identifies risk factors for invasive progression. *Cancer Cell* **41**, 986-1002.e1009, doi:10.1016/j.ccell.2023.04.002 (2023).

24 Barnabas, N. & Cohen, D. Phenotypic and Molecular Characterization of MCF10DCIS and SUM Breast Cancer Cell Lines. *Int J Breast Cancer* **2013**, 872743, doi:10.1155/2013/872743 (2013).

25 Hu, M. *et al.* Regulation of in situ to invasive breast carcinoma transition. *Cancer Cell* **13**, 394-406, doi:10.1016/j.ccr.2008.03.007 (2008).

26 Miller, F. R., Santner, S. J., Tait, L. & Dawson, P. J. MCF10DCIS.com xenograft model of human comedo ductal carcinoma in situ. *J Natl Cancer Inst* **92**, 1185-1186, doi:10.1093/jnci/92.14.1185a (2000).

27 Gan, S. *et al.* Distinct tumor architectures and microenvironments for the initiation of breast cancer metastasis in the brain. *Cancer Cell* **42**, 1693-1712.e1624, doi:10.1016/j.ccell.2024.08.015 (2024).

28 Massagué, J. & Sheppard, D. TGF-β signalling in health and disease. *Cell* **186**, 4007-4037, doi:10.1016/j.cell.2023.07.036 (2023).

29 Siegel, P. M., Shu, W., Cardiff, R. D., Muller, W. J. & Massagué, J. Transforming growth factor beta signalling impairs Neu-induced mammary tumorigenesis while promoting pulmonary metastasis. *Proc Natl Acad Sci U S A* **100**, 8430-8435, doi:10.1073/pnas.0932636100 (2003).

30 Luo, K. Signalling Cross Talk between TGF-β/Smad and Other Signalling Pathways. *Cold Spring Harb Perspect Biol* **9**, doi:10.1101/cshperspect.a022137 (2017).

31 Band, A. M. & Laiho, M. Crosstalk of TGF-β and estrogen receptor signalling in breast cancer. *J Mammary Gland Biol Neoplasia* **16**, 109-115, doi:10.1007/s10911-011-9203-7 (2011).

32 Song, C. Z., Tian, X. & Gelehrter, T. D. Glucocorticoid receptor inhibits transforming growth factor-beta signalling by directly targeting the transcriptional activation function of Smad3. *Proc Natl Acad Sci U S A* **96**, 11776-11781, doi:10.1073/pnas.96.21.11776 (1999).

33 Campeau, E. *et al.* A versatile viral system for expression and depletion of proteins in mammalian cells. *PLoS One* **4**, e6529, doi:10.1371/journal.pone.0006529 (2009).

34 Ye, J. *et al.* Primer-BLAST: A tool to design target-specific primers for polymerase chain reaction. *BMC Bioinformatics* **13**, 134, doi:10.1186/1471-2105-13-134 (2012).

35 Zhang, X. *et al.* A renewable tissue resource of phenotypically stable, biologically and ethnically diverse, patient-derived human breast cancer xenograft models. *Cancer Res* **73**, 4885-4897, doi:10.1158/0008-5472.Can-12-4081 (2013).

36 Behbod, F. *et al.* An intraductal human-in-mouse transplantation model mimics the subtypes of ductal carcinoma in situ. *Breast Cancer Res* **11**, R66, doi:10.1186/bcr2358 (2009).

37 Henneman, L. *et al.* Selective resistance to the PARP inhibitor olaparib in a mouse model for BRCA1-deficient metaplastic breast cancer. *Proc Natl Acad Sci U S A* **112**, 8409-8414, doi:10.1073/pnas.1500223112 (2015).

38 Cardiff, R. D., Moghanaki, D. & Jensen, R. A. Genetically engineered mouse models of mammary intraepithelial neoplasia. *J Mammary Gland Biol Neoplasia* **5**, 421-437, doi:10.1023/a:1009534129331 (2000).

39 Boelens, M. C. *et al.* PTEN Loss in E-Cadherin-Deficient Mouse Mammary Epithelial Cells Rescues Apoptosis and Results in Development of Classical Invasive Lobular Carcinoma. *Cell Rep* **16**, 2087-2101, doi:10.1016/j.celrep.2016.07.059 (2016).

40 Dobin, A. *et al.* STAR: ultrafast universal RNA-seq aligner. *Bioinformatics* **29**, 15-21, doi:10.1093/bioinformatics/bts635 (2013).

41 Haas, B. J. *et al.* Accuracy assessment of fusion transcript detection via read-mapping and de novo fusion transcript assembly-based methods. *Genome Biol* **20**, 213, doi:10.1186/s13059-019-1842-9 (2019).

42 Faul, F., Erdfelder, E., Buchner, A. & Lang, A. G. Statistical power analyses using G*Power 3.1: tests for correlation and regression analyses. *Behav Res Methods* **41**, 1149-1160, doi:10.3758/brm.41.4.1149 (2009).

Supplementary Data

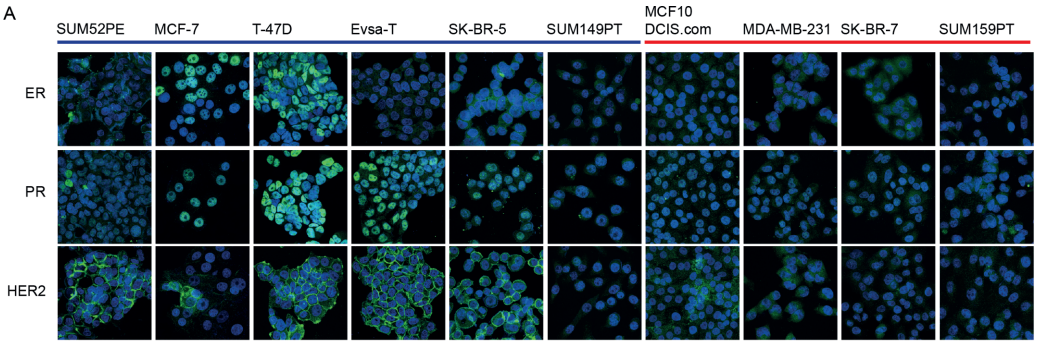

B

Cell line			
Name	**ER**	**PR**	**HER2**
SUM52PE	-	-	+
MCF-7	+	+	-
T-47D	+	+	+
Evsa-T	-	+	+
SK-BR-5	-	-	+
SUM149PT	-	-	-
MCF10DCIS.com	-	-	-
MDA-MB-231	-	-	-
SK-BR-7	-	-	-
SUM159PT	-	-	-

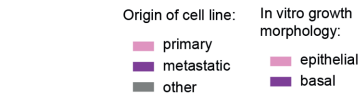

C

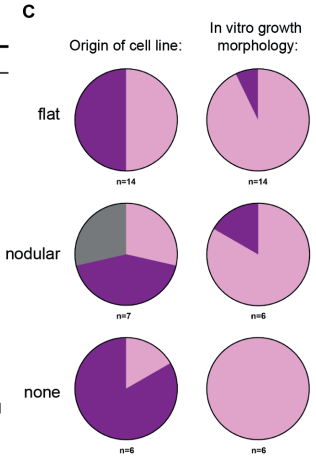

D

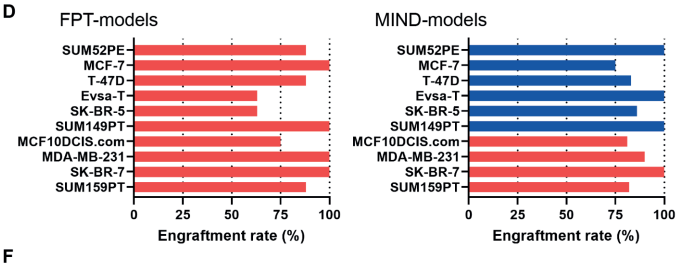

E

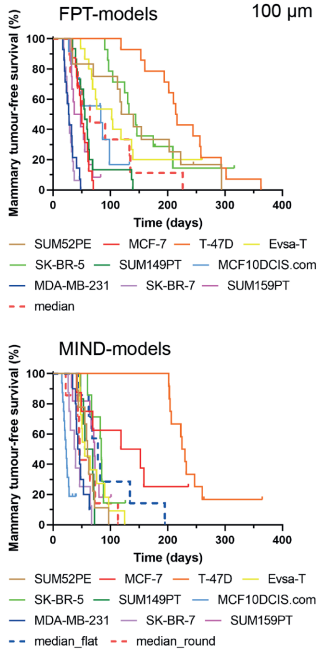

F

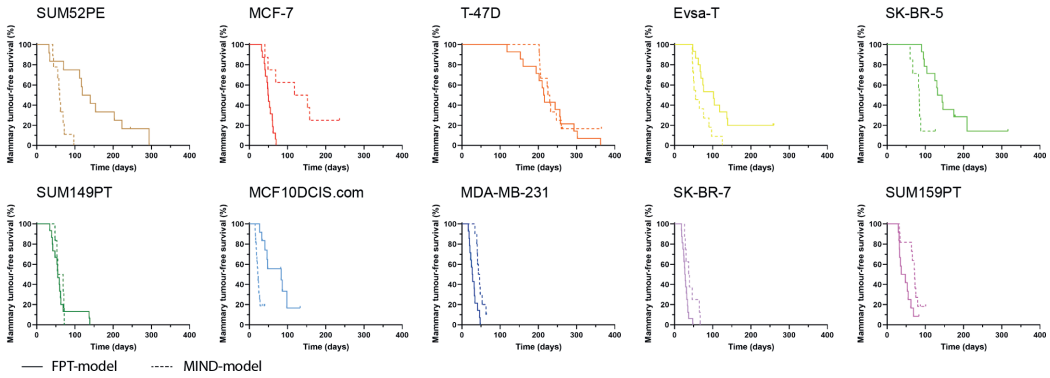

Supplementary Figure 1: Characterisation of BC cell lines and tumour engraftment

A) Immunofluorescence staining for oestrogen receptor (ER), progesterone receptor (PR) and HER2 in MIND-flat models SUM52PE, MCF-7, T47-D, Evsa-T, SK-BR-5, SUM149PT and MIND-nodular models MCF10DCIS.com, MDA-MB-231, SK-BR-7, SUM159PT (scale bar 100 µm). **B**) Summary table of the immunofluorescence analysis (Supplementary Figure 1A) indicating the presence (+) or absence (-) of expression of oestrogen receptor (ER), progesterone receptor (PR) or HER2. **C**) Origin of cell line (primary, metastatic or other (i.e. pleural effusion)) as well as epithelial or basal growth characteristics of the cell line *in vitro* do not determine growth morphology *in vivo*. N-number indicates the amount of cell lines with indicated characteristics. **D**) Engraftment rate (%) for FPT-CDX tumours, showing range of engraftment between 65% (Evsa-T, SK-BR-5) and 100% (MCF-7, SUM149PT, MDA-MB-231, SK-BR-7) and for MIND-engrafted tumours with engraftment rates between 75% (MCF-7) and 100% (SUM52PE, Evsa-T, SUM149PT, SK-BR-7). **E**) Mammary tumour-free survival (%) of mice injected with BC cell lines via the FPT method (upper panel) or the MIND method (lower panel), showing overall longer mammary tumour-free survival in the FPT-CDX models compared to the MIND-CDX models. **F**) Comparison of mammary tumour-free survival (%) listed per cell line and compared between FPT (solid line) and MIND (dashed line).

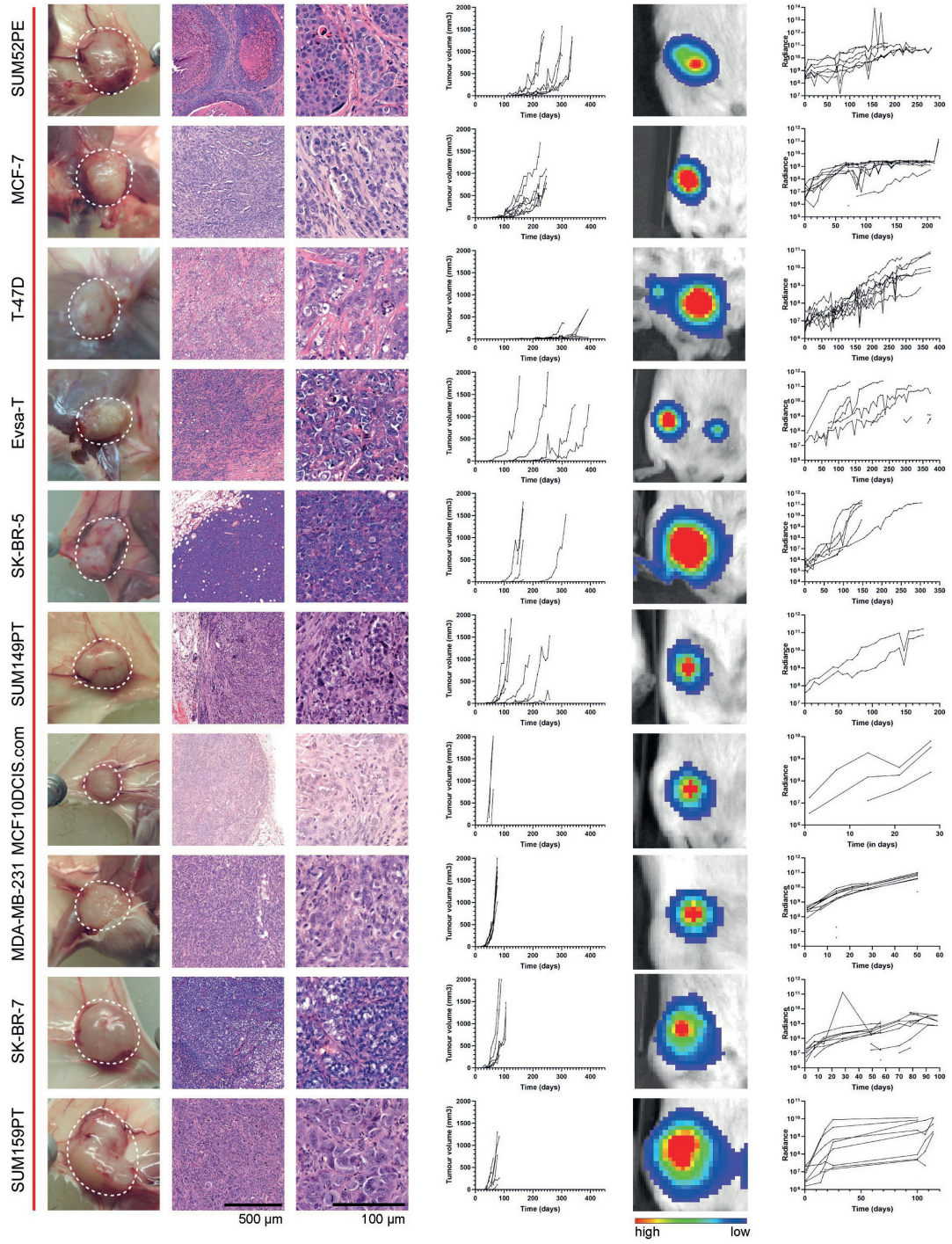
SUM52PE
MCF-7
T-47D
Evsa-T
SK-BR-5
SUM149PT
MCF10DCIS.com
MDA-MB-231
SK-BR-7
SUM159PT
500 µm
100 µm
Tumour volume (mm3)
Time (days)
Radiance
Time (in days)
high
low

Supplementary Figure 2: FPT-CDX tumours show nodular growth only

From left to right, for each cell line: Representative photograph of FPT-CDX tumour; HE staining of corresponding tumour type and HE zoom-in (scale bars 500 µm, zoom-in 100 µm); Tumour growths by tumour volume (mm3) over time (days); representative bioluminescence (BLI) image and tumour growth measurements by BLI radiance over time (days). Red line represents nodular growth pattern.

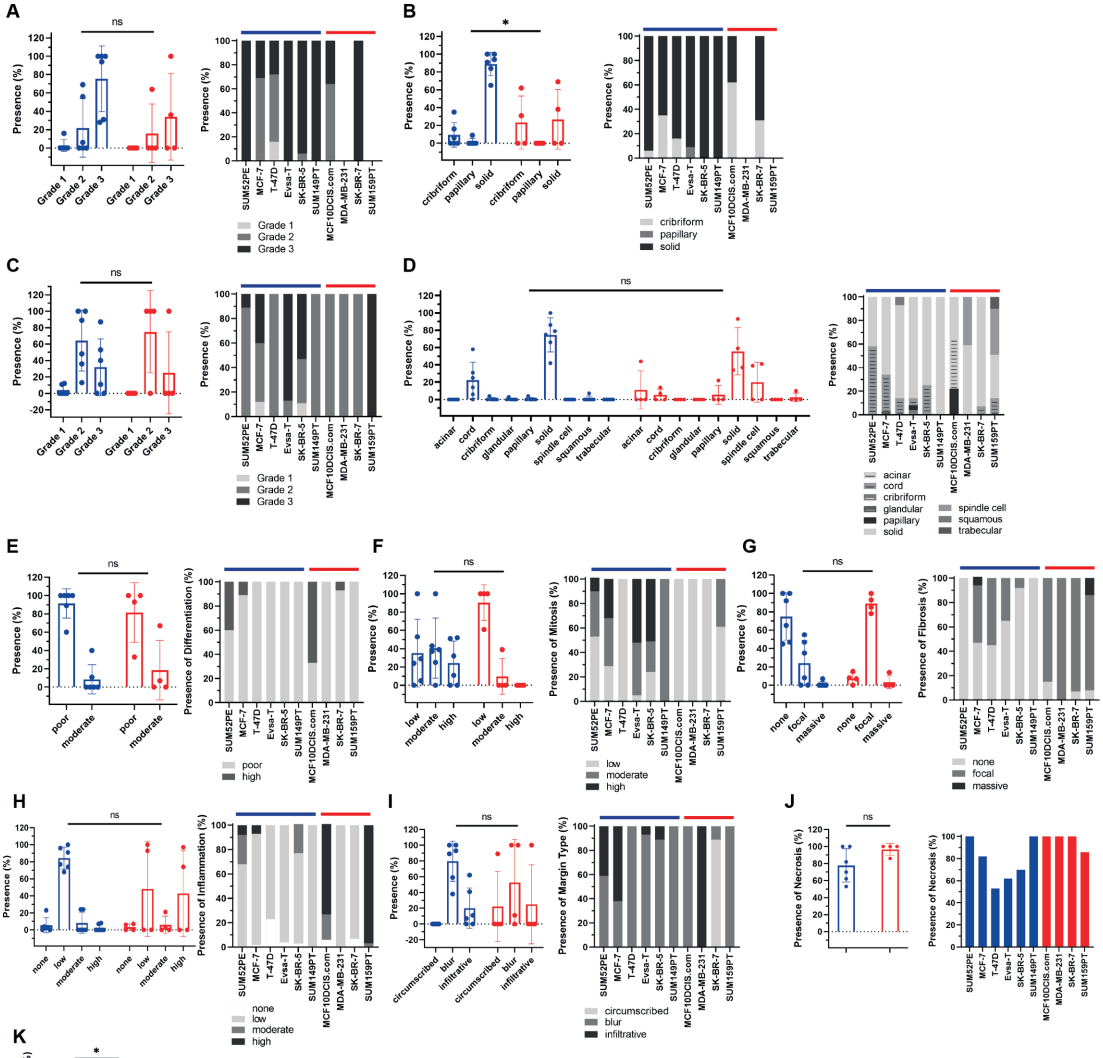
A
B
C
D
E
F
G
H
I
J
K
ns
*
Presence (%)
Grade 1
Grade 2
Grade 3
cribriform
papillary
solid
acinar
cord
glandular
spindle cell
squamous
trabecular
poor
moderate
high
Presence of Differentiation (%)
Presence of Mitosis (%)
low
Presence of Fibrosis (%)
none
focal
massive
Presence of Inflammation (%)
Presence of Margin Type (%)
circumscribed
blur
infiltrative
Presence of Necrosis (%)
Presence of Calcifications (%)
MIND-flat models
MIND-nodular models
SUM52PE
MCF-7
T-47D
Evsa-T
SK-BR-5
SUM149PT
MCF10DCIS.com
MDA-MB-231
SK-BR-7
SUM159PT

Supplementary Figure 3: Pathological analysis of MIND-CDX tumours

A) Tumour grading in MIND-flat (blue) and MIND-nodular lesions (red) diagnosed as DCIS (ns=not significant; Unpaired t-test). **B**) Pathological growth features in MIND-flat (blue) and MIND-nodular (red) DCIS cases (p=0.0212; 2-way ANOVA). **C**) Tumour grading in MIND-flat (blue) and MIND-nodular tumours (red) with IBC (ns=not significant; Unpaired t-test). **D**) Pathological growth features in MIND-flat (blue) and MIND-nodular tumours (red) with IBC (ns=not significant; 2-way ANOVA). **E**) Presence of differentiation in percent in MIND-flat (blue) and MIND-nodular tumours (red) (ns=not significant; 2-way ANOVA). **F**) Presence of mitosis in percent in MIND-flat (blue) and MIND-nodular tumours (red) (ns=not significant; 2-way ANOVA). **G**) Presence of fibrosis in percent in MIND-flat (blue) and MIND-nodular tumours (red) (ns=not significant; 2-way ANOVA). **H**) Presence of inflammation in percent in MIND-flat (blue) and MIND-nodular tumours (red) (ns=not significant; 2-way ANOVA). **I**) Presence of margin type in percent in MIND-flat (blue) and MIND-nodular tumours (red) (ns=not significant; 2-way ANOVA). **J**) Presence of necrosis in percent in MIND-flat (blue) and MIND-nodular tumours (red) (ns=not significant; Unpaired t-test). **K**) Presence of calcifications in MIND-flat (blue) and MIND-nodular tumours (red) (p=0.0159; Unpaired t-test). All figure panels: n=6 for MIND-flat and n=4 for MIND-nodular CDX tumour models.

A

Cell line				MIND Model							
Name	**ER**	**PR**	**HER2**	**Growth Pattern**	**ER**	**PR**	**HER2**	**Ki-67 (%)**	**Casp-3 (%)**	**Average Tumor Onset (days)**	**Average Sacrifice (days)**
SUM52PE	-	-	+	flat	-	-	+	70	5	74	140
MCF-7	+	+	-	flat	+	+	-	60	<1	74	193
T-47D	+	+	+	flat	+	(+)	+	15	1	199	323
Evsa-T	-	+	+	flat	-	+	+	70	<1	82	160
SK-BR-5	-	-	+	flat	-	-	+	40	0	87	125
SUM149PT	-	-	-	flat	-	-	-	90	1	62	109
MCF10DCIS.com	-	-	-	round	-	-	-	70	3	22	38
MDA-MB-231	-	-	-	round	-	-	-	80	<1	45	59
SK-BR-7	-	-	-	round	-	-	-	30	5	38	73
SUM159PT	-	-	-	round	-	-	-	60	<1	59	99

B

Cell line				Fat pad transplantation Model							
Name	**ER**	**PR**	**HER2**	**Growth Pattern**	**ER**	**PR**	**HER2**	**Ki-67 (%)**	**Casp-3 (%)**	**Average Tumor Onset (days)**	**Average Sacrifice (days)**
SUM52PE	-	-	+	round	-	-	+	60	10	135	286
MCF-7	+	+	-	round	+	(+)	-	60	5	51	226
T-47D	+	+	+	round	+	+	+	40	0	226	364*
Evsa-T	-	+	+	round	-	(+)	+	60	0	91	291
SK-BR-5	-	-	+	round	-	-	+	60	<1	133	210
SUM149PT	-	-	-	round	-	-	-	90	<1	64	176
MCF10DCIS.com	-	-	-	round	-	-	-	40	0	50	87
MDA-MB-231	-	-	-	round	-	-	-	80	0	29	77
SK-BR-7	-	-	-	round	-	-	-	20	1	28	106
SUM159PT	-	-	-	round	-	-	-	40	<1	43	80

* not due to tumor growth

C

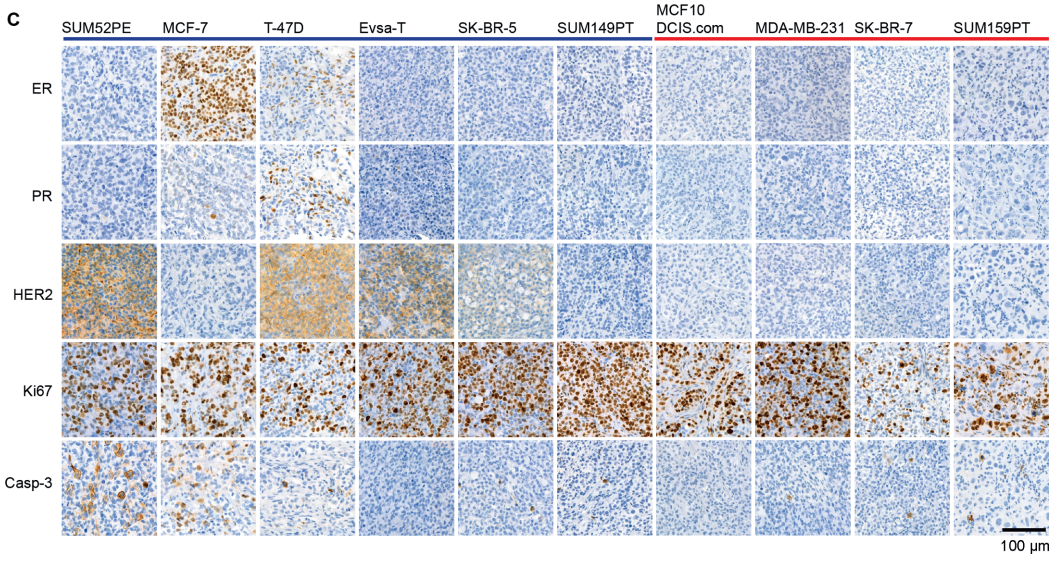

Supplementary Figure 4: Histopathological characterisation of MIND-CDX and FPT-CDX tumours

A) Summary table of MIND-CDX models including their HR status *in vitro*, as well as outgrowth pattern and intra-tumour HR status, Ki-67 and cleaved-caspase 3 positivity in percent, average tumour onset (days) and average sacrifice time (days) *in vivo*. **B**) Summary table of FPT-CDX models including their HR status *in vitro*, as well as outgrowth pattern and intra-tumour HR status, Ki-67 and cleaved-caspase 3 positivity in percent, average tumour onset (days) and average sacrifice time (days) *in vivo*. **C**) IHC staining for tumour subtype classifiers (ER, PR, HER2), proliferation (Ki67) and apoptosis (Cleaved Caspase-3) of FPT-CDX tumours (scale bar 100 µm).

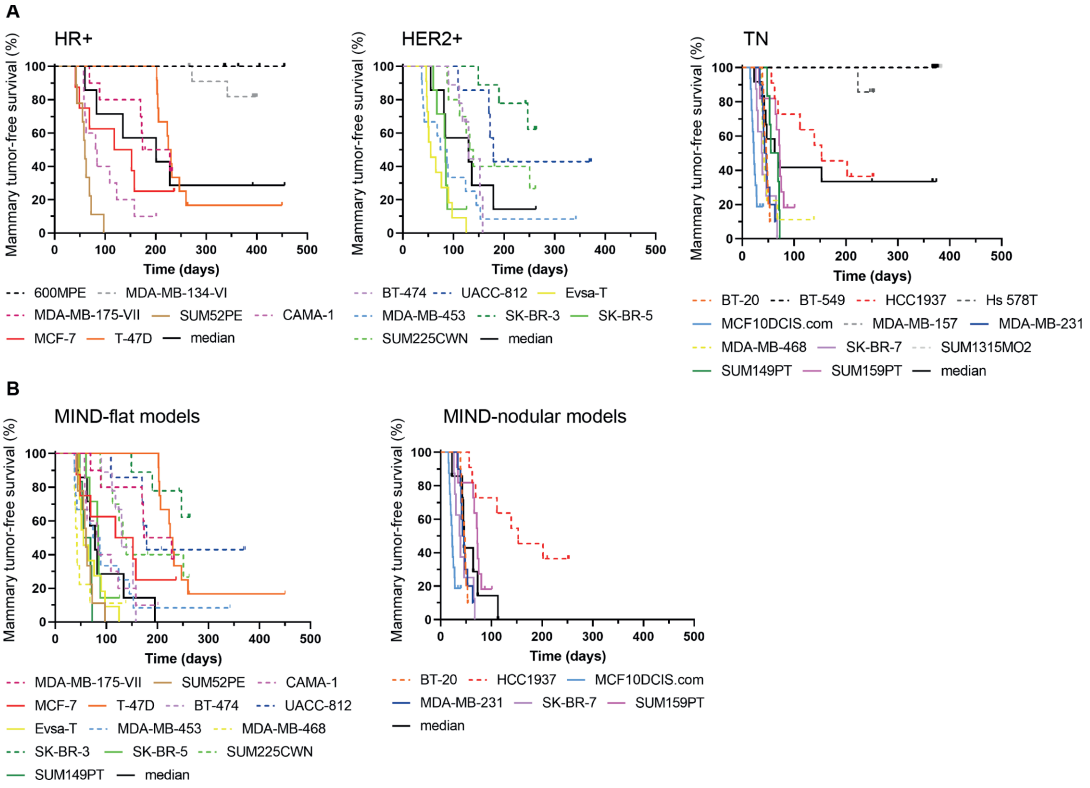
A
HR+
HER2+
TN
Mammary tumor-free survival (%)
Time (days)
600MPE
MDA-MB-134-VI
MDA-MB-175-VII
SUM52PE
CAMA-1
MCF-7
T-47D
median
BT-474
UACC-812
Evsa-T
MDA-MB-453
SK-BR-3
SK-BR-5
SUM225CWN
BT-20
BT-549
HCC1937
Hs 578T
MCF10DCIS.com
MDA-MB-157
MDA-MB-231
MDA-MB-468
SK-BR-7
SUM1315MO2
SUM149PT
SUM159PT
B
MIND-flat models
MIND-nodular models
Mammary tumor-free survival (%)
Time (days)
MDA-MB-175-VII
SUM52PE
CAMA-1
MCF-7
T-47D
BT-474
UACC-812
Evsa-T
MDA-MB-453
MDA-MB-468
SK-BR-3
SK-BR-5
SUM225CWN
SUM149PT
median
BT-20
HCC1937
MCF10DCIS.com
MDA-MB-231
SK-BR-7
SUM159PT
median

Supplementary Figure 5: MIND-CDX tumour growth kinetics correlate with BC cell line subtype but do not determine morphology

A) Mammary tumour-free survival rates (%) of MIND-CDX models grouped according to their HR+, HER2+ or Triple Negative (TN) subtype. **B**) Mammary tumour-free survival rates (%) of MIND-CDX models grouped according to their MIND-flat (left panel) or MIND-nodular (right panel) tumour growth pattern showing that flat tumour growth takes on average longer compared to nodular growth.

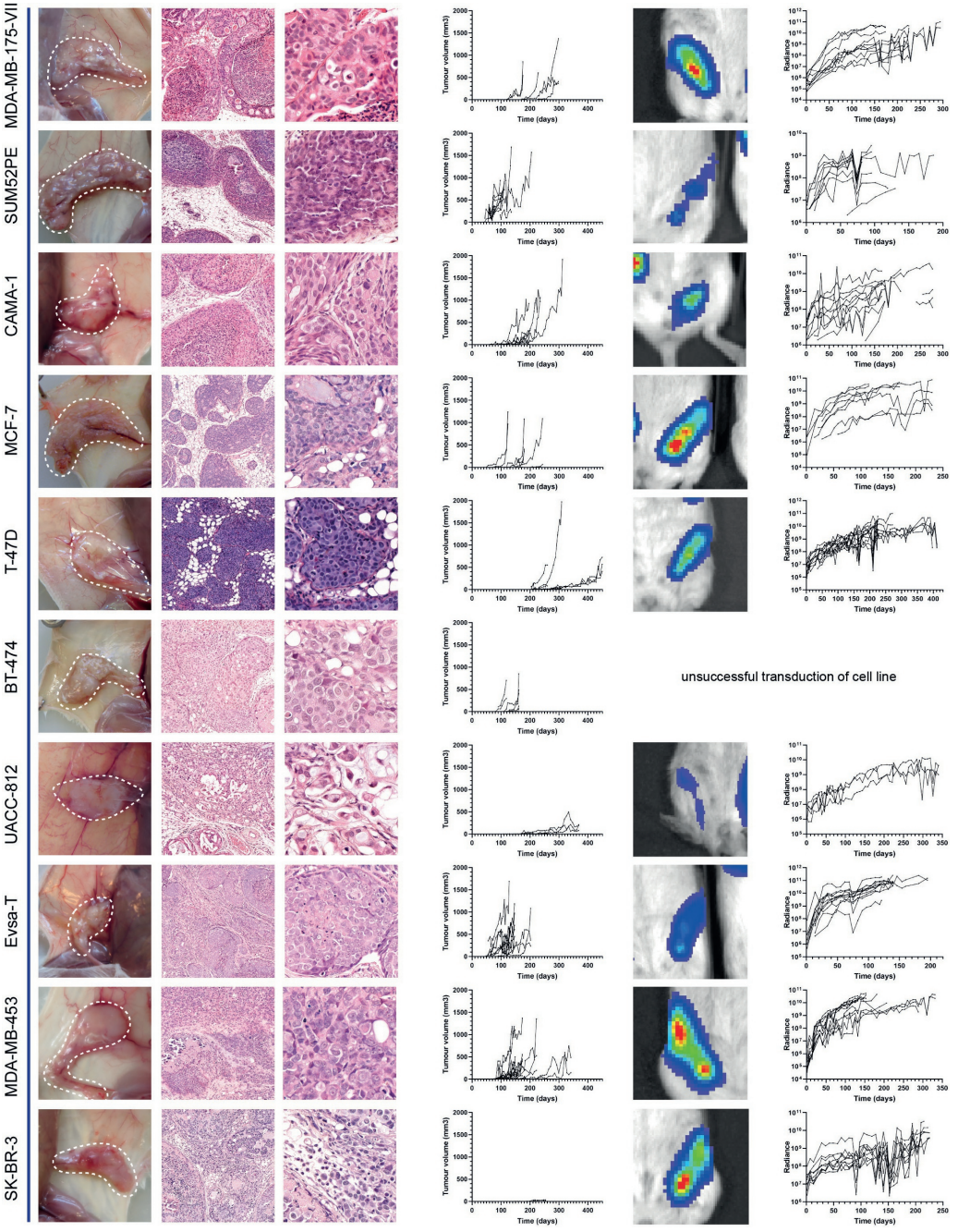
MDA-MB-175-VII
SUM52PE
CAMA-1
MCF-7
T-47D
BT-474
UACC-812
Evsa-T
MDA-MB-453
SK-BR-3
Tumour volume (mm3)
Time (days)
Radiance
unsuccessful transduction of cell line

Supplementary Figure 6: Difference in tumour growth pattern in MIND-CDX models

From left to right, for each cell line: Representative photograph of MIND-tumour; HE staining of corresponding tumour type and HE zoom-in (scale bars 500 µm, zoom-in 100 µm); Tumour volume (mm3) over time (days); representative bioluminescence (BLI) image and tumour growth measurements by BLI radiance over time (days). Blue line represents flat and red line nodular growth pattern.

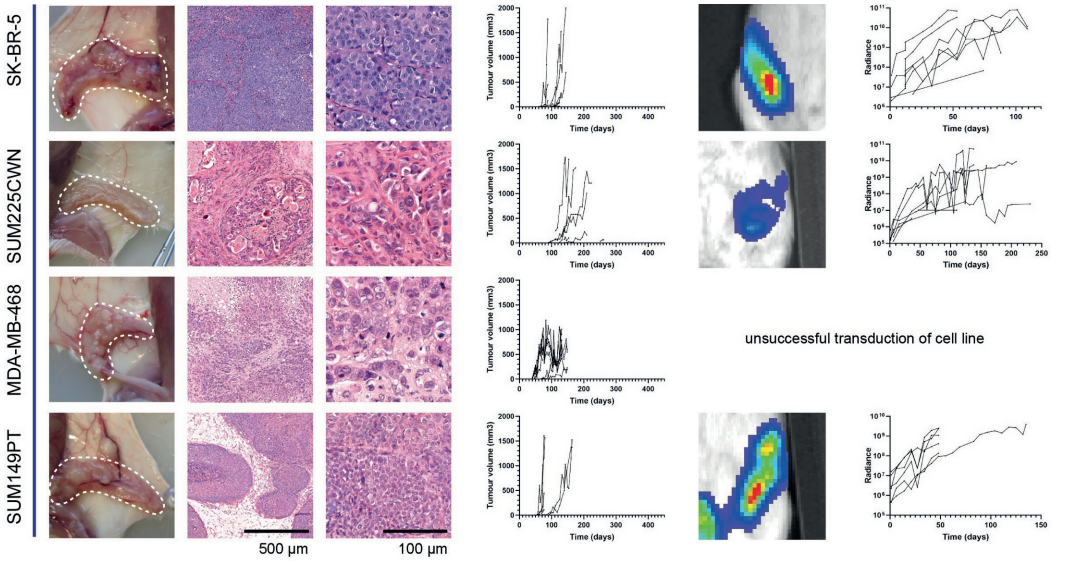
SK-BR-5
SUM225CWN
MDA-MB-468
SUM149PT
Tumour volume (mm3)
Time (days)
Radiance
unsuccessful transduction of cell line
500 µm
100 µm

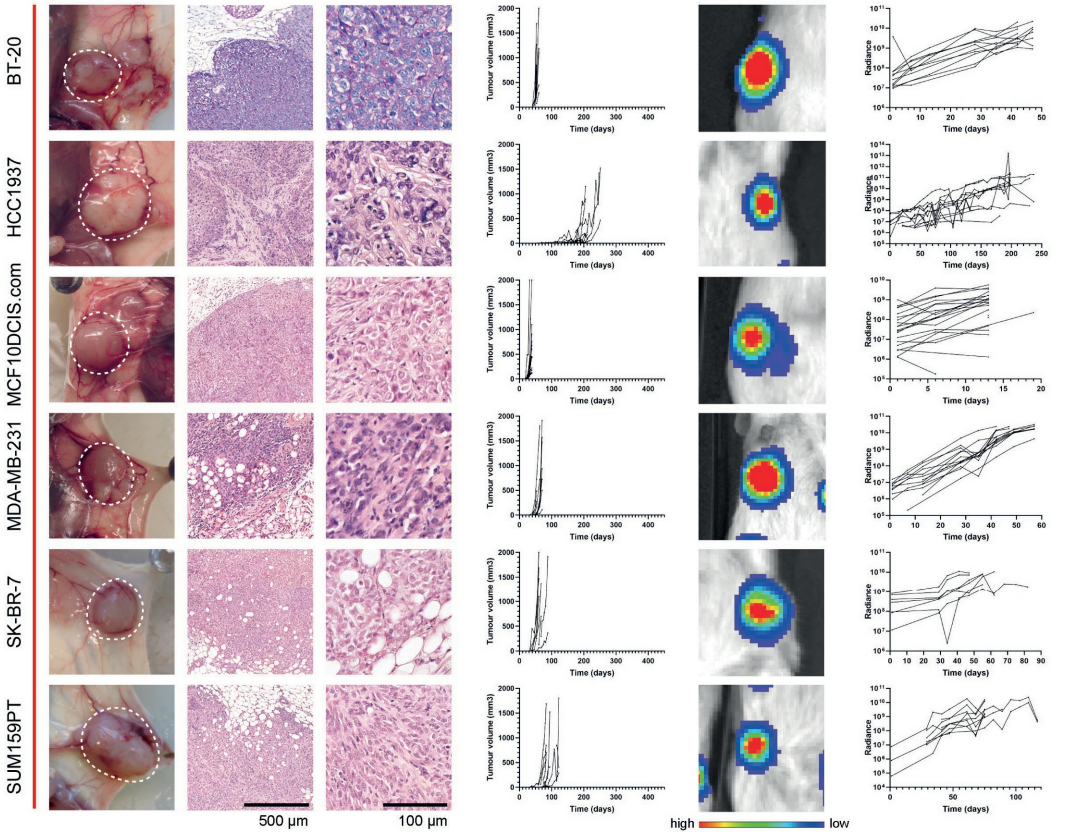
BT-20
HCC1937
MCF10DCIS.com
MDA-MB-231
SK-BR-7
SUM159PT
Tumour volume (mm3)
Time (days)
Radiance
500 µm
100 µm
high
low

Supplementary Figure 7 (continuation of Supplementary Figure 6): Difference in tumour growth pattern in MIND-CDX models

From left to right, for each cell line: Representative photograph of MIND-tumour; HE staining of corresponding tumour type and HE zoom-in (scale bars 500 µm, zoom-in 100 µm); Tumour volume (mm3) over time (days); representative bioluminescence (BLI) image and tumour growth measurements by BLI radiance over time (days). Blue line represents flat and red line nodular growth pattern.

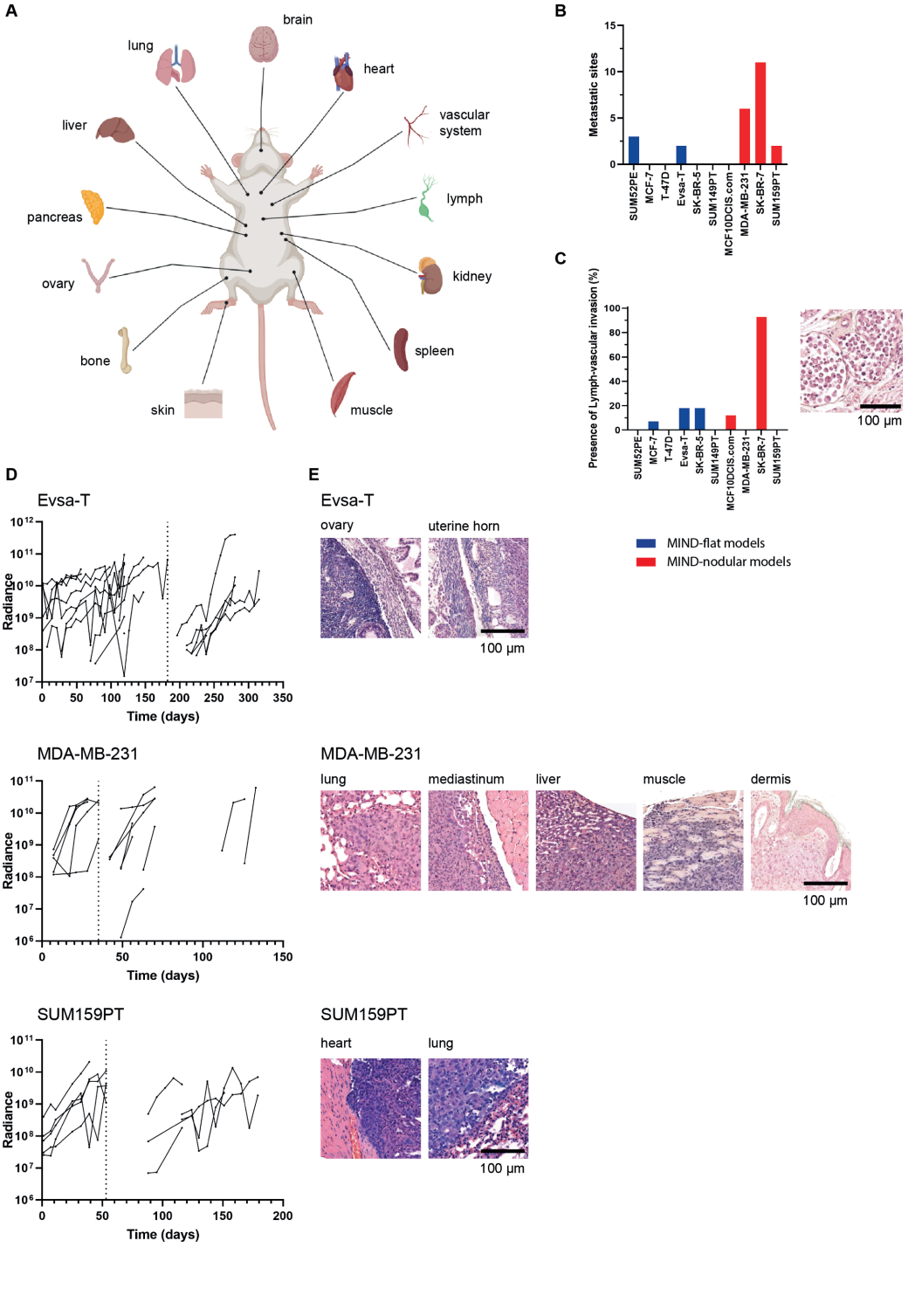
A
brain
lung
heart
liver
vascular system
lymph
pancreas
ovary
kidney
bone
spleen
skin
muscle
B
Metastatic sites
SUM52PE
MCF-7
T-47D
Evsa-T
SK-BR-5
SUM149PT
MCF10DCIS.com
MDA-MB-231
SK-BR-7
SUM159PT
C
Presence of Lymph-vascular invasion (%)
100 µm
MIND-flat models
MIND-nodular models
D
Evsa-T
Radiance
Time (days)
MDA-MB-231
SUM159PT
E
Evsa-T
ovary
uterine horn
100 µm
MDA-MB-231
lung
mediastinum
liver
muscle
dermis
100 µm
SUM159PT
heart
lung
100 µm

Supplementary Figure 8: Nodular-growing MIND-CDX tumours have increased metastatic potential

A) Overview of mouse organs investigated for the presence of metastases. **B**) Number of metastatic sites per cell line, showing that more metastatic sites were detected for MIND-nodular tumours compared to MIND-flat tumours. **C**) Presence of lymph-vascular invasion (%) based on HE staining (example image on the right depicts tumour cell presence in dilated lymphatic vessel). Lymph-vascular invasion was detected in both MIND-flat (blue) and MIND-nodular (red) tumours, with SK-BR-7 showing the highest frequency of occurrence. **D**) Metastatic growth measured by BLI over time (days) of MIND-flat Evsa-T tumours and MIND-nodular MDA-MB-231 and SUM159PT tumours. **E**) HE stainings of metastatic lesions from different organ sites of MIND-flat Evsa-T tumours and MIND-nodular MDA-MB-231 and SUM159PT tumours (scale bar 100 µm).

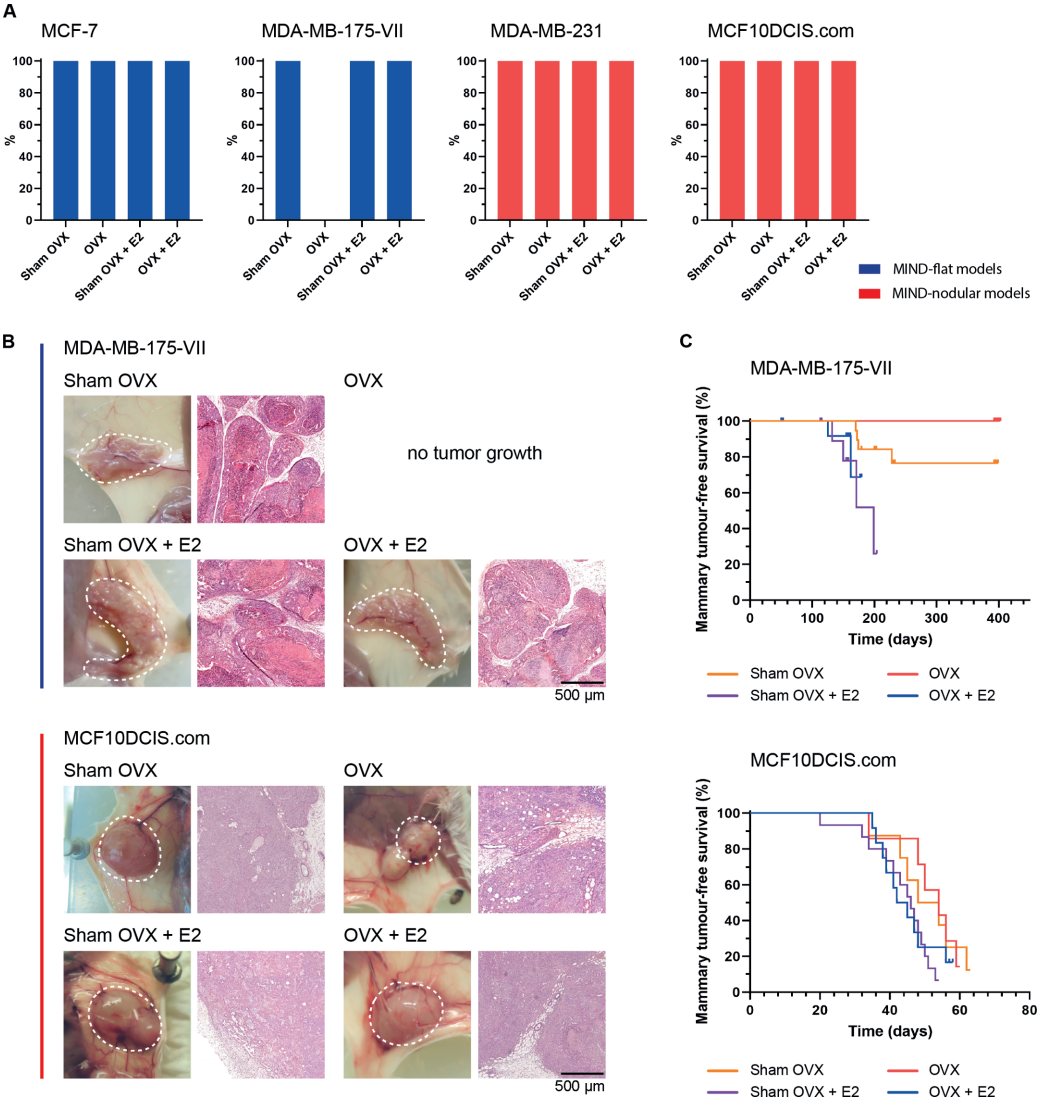
A
MCF-7
MDA-MB-175-VII
MDA-MB-231
MCF10DCIS.com
%
100
80
60
40
20
0
Sham OVX
OVX
Sham OVX + E2
OVX + E2
MIND-flat models
MIND-nodular models
B
MDA-MB-175-VII
Sham OVX
OVX
no tumor growth
Sham OVX + E2
OVX + E2
500 µm
MCF10DCIS.com
Sham OVX
OVX
Sham OVX + E2
OVX + E2
500 µm
C
MDA-MB-175-VII
Mammary tumour-free survival (%)
Time (days)
Sham OVX
OVX
Sham OVX + E2
OVX + E2
MCF10DCIS.com
Mammary tumour-free survival (%)
Time (days)
Sham OVX
OVX
Sham OVX + E2
OVX + E2

Supplementary Figure 9: Oestrogen influences growth kinetics but not morphology of MIND-CDX tumours

A) MIND-CDX models of ER+ cell lines MCF-7 and MDA-MB-175-VII do not show differences in tumour growth morphology when animals are sham-ovariectomised (Sham OVX), ovariectomised (OVX) and therefore oestrogen-depleted, or supplemented with oestrogen (Sham OVX + E2 and OVX + E2). All tumour outgrowths show a flat growth pattern. Graphs show the frequency of growth pattern occurrence (%); MCF-7: n=12 for Sham OVX, n=5 for OVX, n=11 for Sham OVX + E2, and n=14 for OVX + E2; MDA-MB-175-VII: n=4 for Sham OVX, n=0 for OVX, n=4 for Sham OVX + E2, and n=2 for OVX + E2. MDA-MB-175-VII cell line xenografts did not show any tumour growth upon ovariectomy. MIND-CDX models of ER-negative cell lines MDA-MB-231 and MCF10DCIS.com equally do not show differences in tumour growth morphology upon hormone perturbations. All tumours show a nodular growth pattern. Graphs depict the frequency of growth pattern occurrence (%); MDA-MB-231: n=17 for Sham OVX, n=6 for OVX, n=12 for Sham OVX + E2, and n=13 for OVX + E2; MCF10DCIS.com: n=7 for Sham OVX, n=6 for OVX, n=14 for Sham OVX + E2, and n=10 for OVX + E2. **B**) Representative photographs and HE stainings showing no changes in growth pattern morphologies of MIND-flat MDA-MB-175-VII (upper panel) and MIND-nodular MCF10DCIS.com (lower panel) tumours after ovariectomy (OVX) or in non-ovariectomised (Sham OVX) controls, with or without supplementation of oestrogen (E2) (scale bars 500 µm). **C**) Tumour growth kinetics are affected by oestrogen as depicted by the mammary tumour-free survival (%) of MDA-MB-175-VII (upper panel) and MCF10DCIS.com (lower panel) tumours after ovariectomy (OVX) or in non-ovariectomised (Sham OVX) controls, with or without supplementation of oestrogen (E2).

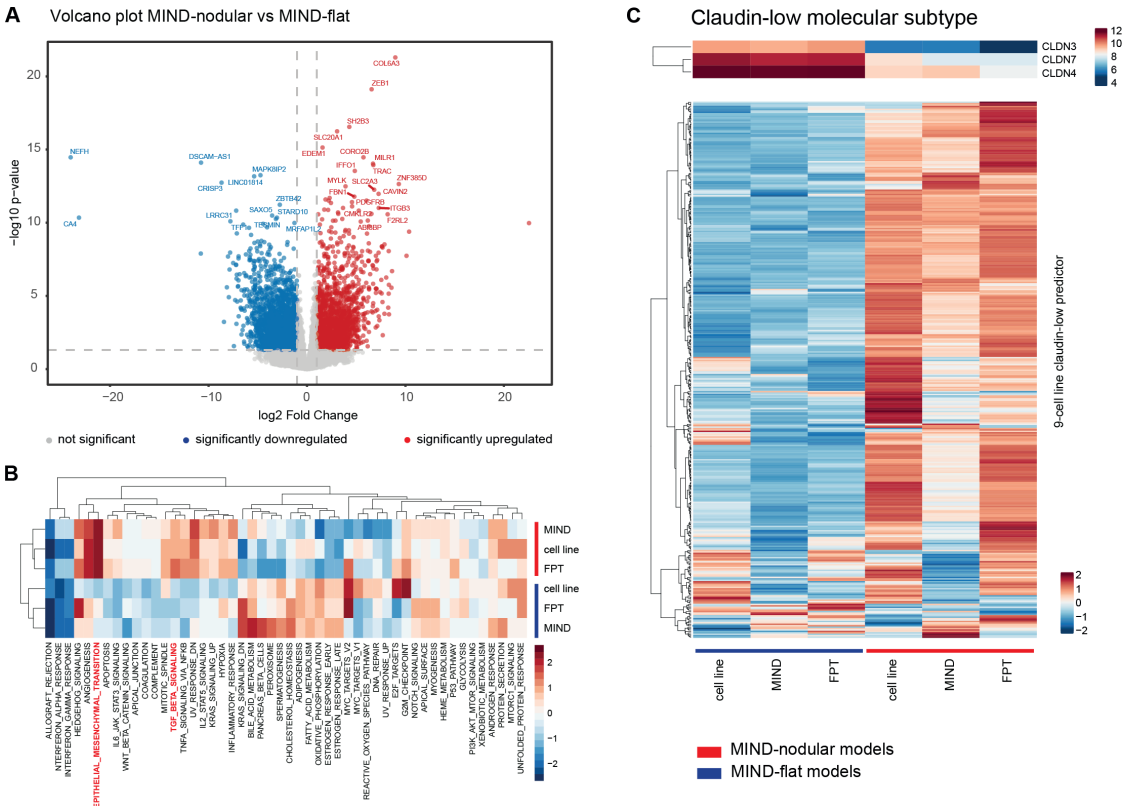
A
Volcano plot MIND-nodular vs MIND-flat
−log10 p-value
log2 Fold Change
not significant
significantly downregulated
significantly upregulated
B
MIND
cell line
FPT
cell line
FPT
MIND
C
Claudin-low molecular subtype
CLDN3
CLDN7
CLDN4
9-cell line claudin-low predictor
cell line
MIND
FPT
cell line
MIND
FPT
MIND-nodular models
MIND-flat models

Supplementary Figure 10: Transcriptomic analysis identifies upregulated EMT and TGF-β signalling in nodular MIND-CDX tumours

A) Volcano plot representing differential gene expression results between models of flat and round morphology. The x-axis indicates the log2 fold change, with downregulated genes to the left and upregulated genes to the right. The y-axis shows the negative logarithm of the adjusted p-value (-log10 adjusted p-value), with higher values indicating greater statistical significance. Blue dots represent genes significantly downregulated, red dots represent genes significantly upregulated, and grey dots indicate genes with no significant change in expression. Top 50 genes based on significance are labelled with their respective gene symbols. **B**) Heat map of hallmark pathways across different models providing a visualization of GSVA scores. Each column of the heat map represents a hallmark pathway, while each row corresponds to a model and growth morphology. The colour scale indicates the GSVA score, where deep blue marks lower activity and deep red signifies higher activity of the pathway in the respective models. EMT and TGF-β pathway signalling are highlighted in red. **C**) Expression of claudins (top part) and heat map of genes included in 9-cell line claudin-low classifier (bottom part) in MIND-flat vs MIND-nodular tumours. Scale bars depicts raw expression for claudins and normalised z-score values for cell-line classifier.

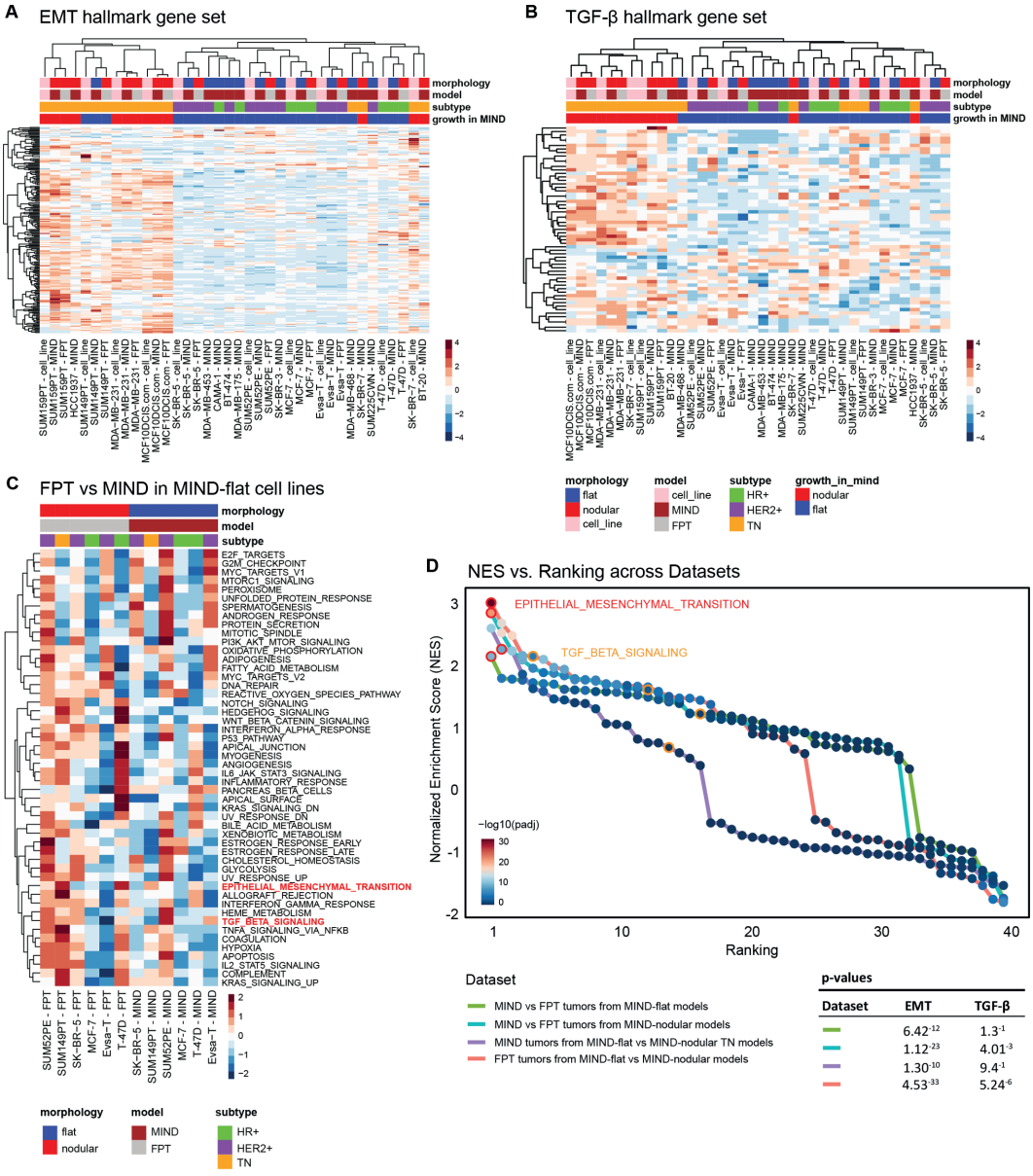
A
EMT hallmark gene set
morphology
model
subtype
growth in MIND
B
TGF-β hallmark gene set
morphology
model
subtype
growth in MIND
morphology
flat
nodular
cell_line
model
cell_line
MIND
FPT
subtype
HR+
HER2+
TN
growth_in_mind
nodular
flat
C
FPT vs MIND in MIND-flat cell lines
morphology
model
subtype
E2F_TARGETS
G2M_CHECKPOINT
MYC_TARGETS_V1
MTORC1_SIGNALING
PEROXISOME
UNFOLDED_PROTEIN_RESPONSE
SPERMATOGENESIS
ANDROGEN_RESPONSE
PROTEIN_SECRETION
MITOTIC_SPINDLE
PI3K_AKT_MTOR_SIGNALING
OXIDATIVE_PHOSPHORYLATION
ADIPOGENESIS
FATTY_ACID_METABOLISM
MYC_TARGETS_V2
DNA_REPAIR
REACTIVE_OXYGEN_SPECIES_PATHWAY
NOTCH_SIGNALING
HEDGEHOG_SIGNALING
WNT_BETA_CATENIN_SIGNALING
INTERFERON_ALPHA_RESPONSE
P53_PATHWAY
APICAL_JUNCTION
MYOGENESIS
ANGIOGENESIS
IL6_JAK_STAT3_SIGNALING
INFLAMMATORY_RESPONSE
PANCREAS_BETA_CELLS
APICAL_SURFACE
KRAS_SIGNALING_DN
UV_RESPONSE_DN
BILE_ACID_METABOLISM
XENOBIOTIC_METABOLISM
ESTROGEN_RESPONSE_EARLY
ESTROGEN_RESPONSE_LATE
CHOLESTEROL_HOMEOSTASIS
GLYCOLYSIS
UV_RESPONSE_UP
EPITHELIAL_MESENCHYMAL_TRANSITION
ALLOGRAFT_REJECTION
INTERFERON_GAMMA_RESPONSE
HEME_METABOLISM
TGF_BETA_SIGNALING
TNFA_SIGNALING_VIA_NFKB
COAGULATION
HYPOXIA
APOPTOSIS
IL2_STAT5_SIGNALING
COMPLEMENT
KRAS_SIGNALING_UP
SUM52PE - FPT
SUM149PT - FPT
SK-BR-5 - FPT
MCF-7 - FPT
Evsa-T - FPT
T-47D - FPT
SK-BR-5 - MIND
SUM149PT - MIND
SUM52PE - MIND
MCF-7 - MIND
T-47D - MIND
Evsa-T - MIND
morphology
flat
nodular
model
MIND
FPT
subtype
HR+
HER2+
TN
D
NES vs. Ranking across Datasets
EPITHELIAL_MESENCHYMAL_TRANSITION
TGF_BETA_SIGNALING
Normalized Enrichment Score (NES)
−log10(padj)
Ranking
Dataset
MIND vs FPT tumors from MIND-flat models
MIND vs FPT tumors from MIND-nodular models
MIND tumors from MIND-flat vs MIND-nodular TN models
FPT tumors from MIND-flat vs MIND-nodular models
p-values
Dataset
EMT
TGF-β
6.42-12
1.3-1
1.12-23
4.01-3
1.30-10
9.4-1
4.53-33
5.24-6

Supplementary Figure 11: Nodular growth is associated with both autocrine and paracrine TGF-β signalling

A+B) Heat maps representing the expression levels of all genes within the EMT (A) and TGF-β pathways (B) across different cell lines and models. Each row represents a gene, and each column represents a sample, with cell line and model information combined as column names. The colour scale, from blue to red, indicates gene expression levels, with blue representing lower expression and red representing higher expression. Rows are scaled to highlight relative expression levels within genes. Annotations for growth conditions, model types, subtypes, and morphologies are provided alongside the corresponding columns. Clustering is based on correlation distance, grouping similar expression patterns together. **C**) GSVA heat map of hallmark pathways comparing the 6 MIND-flat models between transplantation site. The FPT tumours show upregulation of EMT and TGF-β pathway signatures compared to their MIND counterparts. Each row of the heat map represents a hallmark pathway, while each column corresponds to a sample. The colour scale indicates the GSVA score, where deep blue marks lower activity and deep red signifies higher activity of the pathway in the respective sample. The hierarchical clustering is based on correlation, categorizing both samples and pathways based on their activity patterns. Scale below the figure depicts normalized (z-score) GSEA score values. **D**) Dot plot displaying the results of gene set enrichment analysis (GSEA) for upregulated pathways in different datasets: MIND vs FPT tumours from MIND-flat models (green), MIND vs FPT tumours from MIND-nodular models (blue), MIND tumours from MIND-flat vs MIND-nodular TN models (purple), and FPT tumours from MIND-flat vs MIND-nodular models (red). The y-axis lists the Normalized Enrichment Score (NES) for the various comparisons, the x-axis shows the Ranking of the different hallmark gene sets. Dot size represents adjusted p-value and dot colour indicates significance. P-values for EMT and TGF-β in the different dataset comparisons are highlighted in a table.

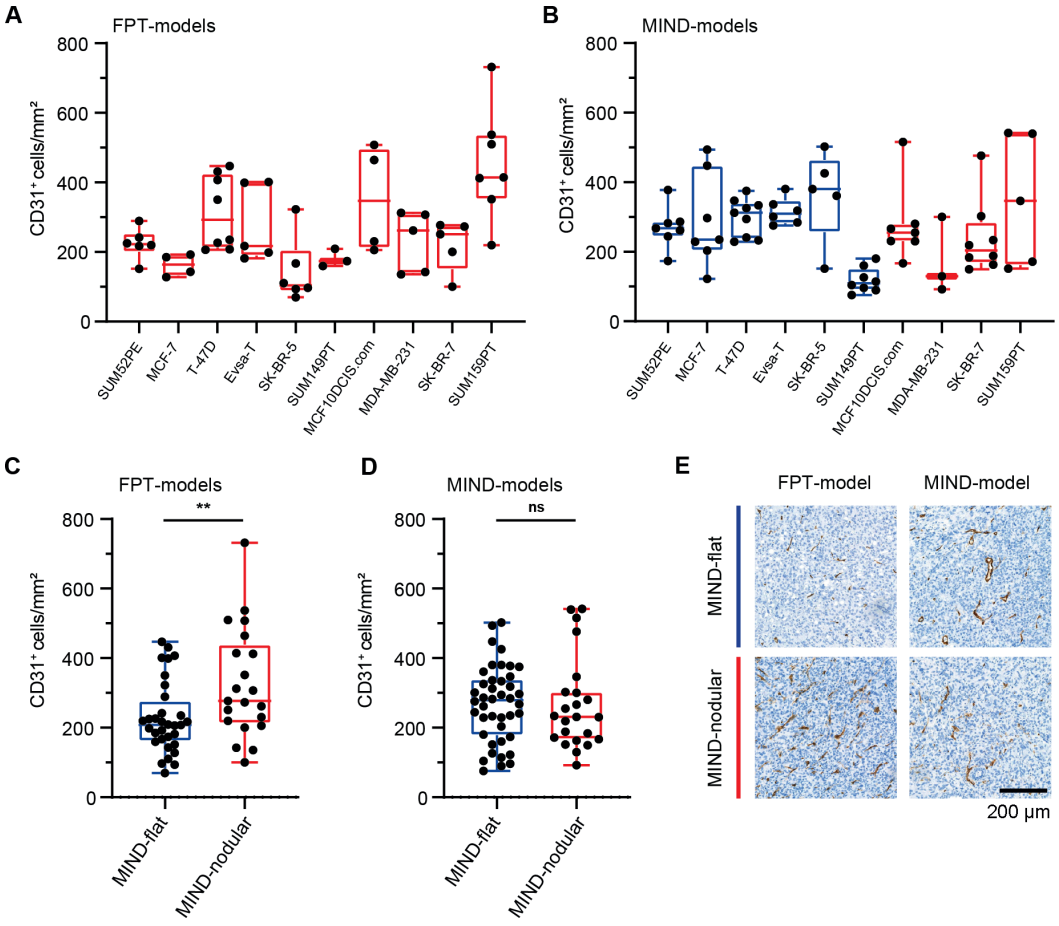
A
FPT-models
CD31⁺ cells/mm²
800
600
400
200
0
SUM52PE
MCF-7
T-47D
Evsa-T
SK-BR-5
SUM149PT
MCF10DCIS.com
MDA-MB-231
SK-BR-7
SUM159PT
B
MIND-models
CD31⁺ cells/mm²
800
600
400
200
0
SUM52PE
MCF-7
T-47D
Evsa-T
SK-BR-5
SUM149PT
MCF10DCIS.com
MDA-MB-231
SK-BR-7
SUM159PT
C
FPT-models
**
CD31⁺ cells/mm²
800
600
400
200
0
MIND-flat
MIND-nodular
D
MIND-models
ns
CD31⁺ cells/mm²
800
600
400
200
0
MIND-flat
MIND-nodular
E
FPT-model
MIND-model
MIND-flat
MIND-nodular
200 µm

Supplementary Figure 12: Angiogenesis in MIND tumours does not correlate with growth morphology

A) Analysis of CD31+ -stained cells per mm2 of tumour mass in FPT shows differences between cell lines. Each dot represents one tumour. Boxes depict minimum to maximum values with mean. **B**) Analysis of CD31+ -stained cells per mm2 of tumour mass in MIND shows differences between cell lines but not within growth morphologies. Each dot represents one tumour. Boxes depict minimum to maximum values with mean. **C**) Cumulative CD31+ -stained cells in FPT tumours measured per mm2 and compared between MIND-flat and MIND-nodular tumours. MIND-nodular lesions present with higher amounts of CD31+ cells per mm2 (p=0.0084; Unpaired t-test). **D**) Cumulative CD31+ -stained cells in MIND tumours measured per mm2 and compared between MIND-flat and MIND-nodular tumours show no significant difference (p=0.9560; Unpaired t-test). **E**) Representative IHC CD31 stainings of FPT and MIND lesions with different growth morphology (scale bar 200 µm).

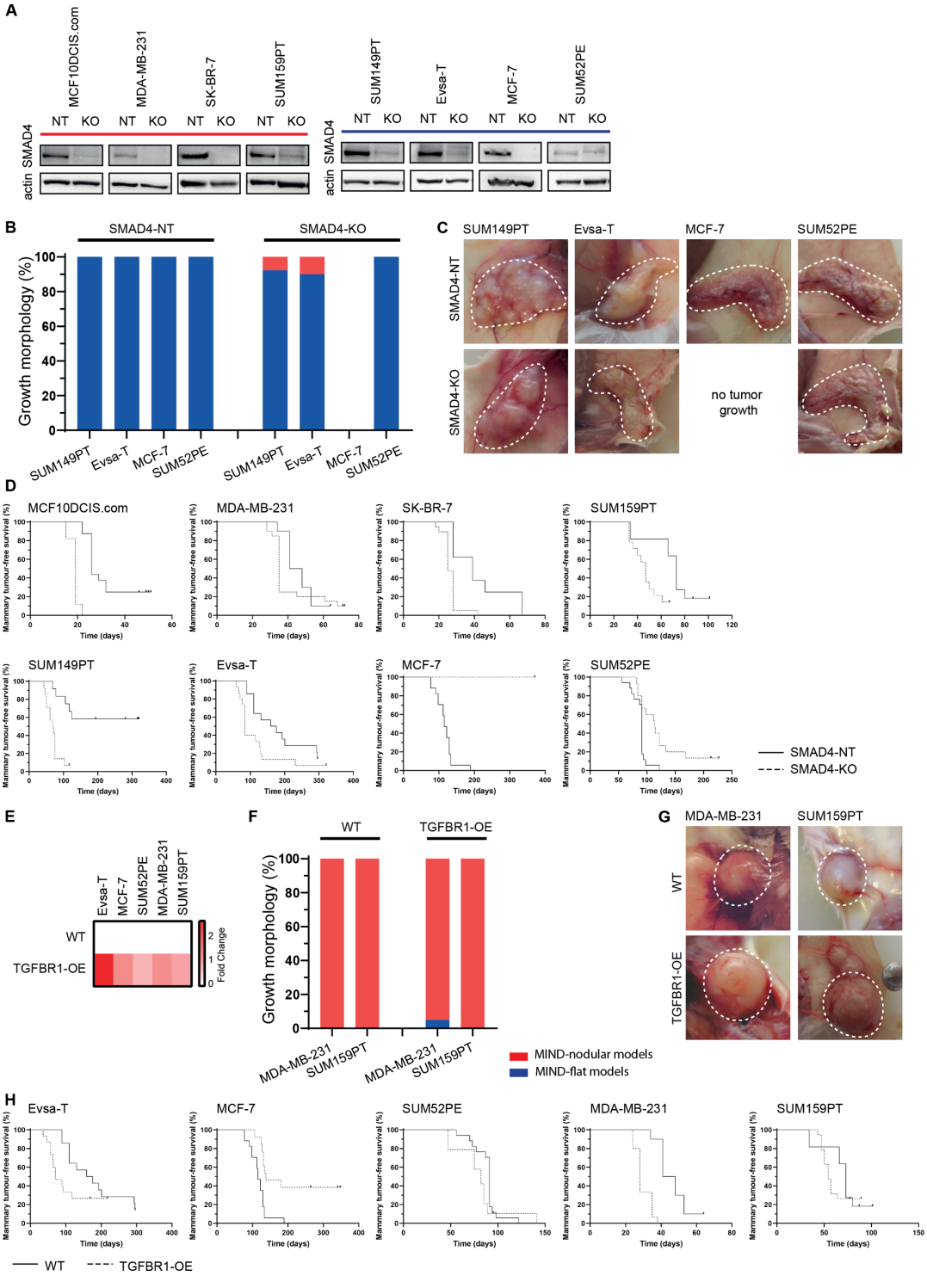
A
MCF10DCIS.com
MDA-MB-231
SK-BR-7
SUM159PT
SUM149PT
Evsa-T
MCF-7
SUM52PE
NT KO NT KO NT KO NT KO
NT KO NT KO NT KO NT KO
SMAD4
actin
B
SMAD4-NT
SMAD4-KO
Growth morphology (%)
SUM149PT
Evsa-T
MCF-7
SUM52PE
C
SUM149PT
Evsa-T
MCF-7
SUM52PE
SMAD4-NT
SMAD4-KO
no tumor growth
D
MCF10DCIS.com
MDA-MB-231
SK-BR-7
SUM159PT
SUM149PT
Evsa-T
MCF-7
SUM52PE
Mammary tumour-free survival (%)
Time (days)
SMAD4-NT
SMAD4-KO
E
Evsa-T
MCF-7
SUM52PE
MDA-MB-231
SUM159PT
WT
TGFBR1-OE
Fold Change
F
WT
TGFBR1-OE
Growth morphology (%)
MDA-MB-231
SUM159PT
MIND-nodular models
MIND-flat models
G
MDA-MB-231
SUM159PT
WT
TGFBR1-OE
H
Evsa-T
MCF-7
SUM52PE
MDA-MB-231
SUM159PT
Mammary tumour-free survival (%)
Time (days)
WT
TGFBR1-OE

Supplementary Figure 13: TGF-β signalling determines MIND-CDX tumour growth kinetics and morphology

A) Western blot analysis for SMAD4 showing downregulation for SMAD4 in knockout (KO) lines compared to cells transduced with a non-targeting control sgRNA (NT) of MIND-nodular cell lines MCF10DCIS.com, MDA-MB-231, SUM159PT and MIND-flat cell lines SUM149PT, Evsa-T, MCF-7, SUM52PE. Actin was used as loading control. **B**) SMAD4 inactivation does not change the growth pattern of already MIND-flat models SUM149PT, Evsa-T, MCF-7, and SUM52PE in MIND-CDX tumours. Graphs show the frequency of growth pattern occurrence (nodular vs flat, %): SMAD4-NT: SUM149PT: 0 (n=0) vs 100 (n=6), Evsa-T: 0 (n=0) vs 100 (n=10), MCF-7: 0 (n=0) vs 100 (n=13), SUM52PE: 0 (n=0) vs 100 (n=17) and SMAD4-KO: SUM149PT: 8 (n=1) vs 92 (n=12), Evsa-T: 10 (n=1) vs 90 (n=9), MCF-7: no tumour growth upon SMAD4-KO, SUM52PE: 0 (n=0) vs 100 (n=14). **C**) Representative photographs of SMAD-NT (upper row) and SMAD-KO (lower row) MIND-CDX tumours from SUM149PT, Evsa-T, MCF-7, and SUM52PE models, showing that originally MIND-flat tumours retain their growth morphology upon SMAD4-KO. **D**) Mammary tumour-free survival (%) of MIND-models injected with SMAD4-NT and SMAD4-KO derivatives of MCF10DCIS.com, MDA-MB-231, SK-BR-7, SUM159PT, SUM149PT, Evsa-T, MCF-7 and SUM52PE cell lines. SMAD4-KO tumours on average showed faster outgrowth compared to controls. MCF-7 SMAD4-KO transplants did not lead to any tumour growth. **E**) Quantitative RT-PCR confirms TGFBR1-OE in modified cell lines compared to their WT counterpart. **F**) TGFBR1-OE does not change the growth pattern of already MIND-nodular models MDA-MB-231, and SUM159PT in MIND-CDX tumours. Graphs show the frequency of growth pattern occurrence (flat vs nodular, %): TGFBR1-WT: MDA-MB-231: 0 (n=0) vs 100 (n=11), SUM159PT: 0 (n=0) vs 100 (n=9), and TGFBR1-OE: MDA-MB-231: 5 (n=1) vs 95 (n=19), SUM159PT: 0 (n=0) vs 100 (n=22). **G**) Representative photographs of TGFBR1-WT (upper row) and TGFBR1-OE (lower row) MIND-CDX tumours from MDA-MB-231 and SUM159PT models, showing that originally MIND-nodular tumours retain their growth morphology upon TGFBR1-OE. **H**) Mammary tumour-free survival (%) of MIND-models injected with Evsa-T, MCF-7, SUM52PE, MDA-MB-231, and SUM159PT cells with/without expression of constitutively active TGFBR1. TGFBR1-OE does not lead to a clear in- or decrease in tumour growth kinetics.

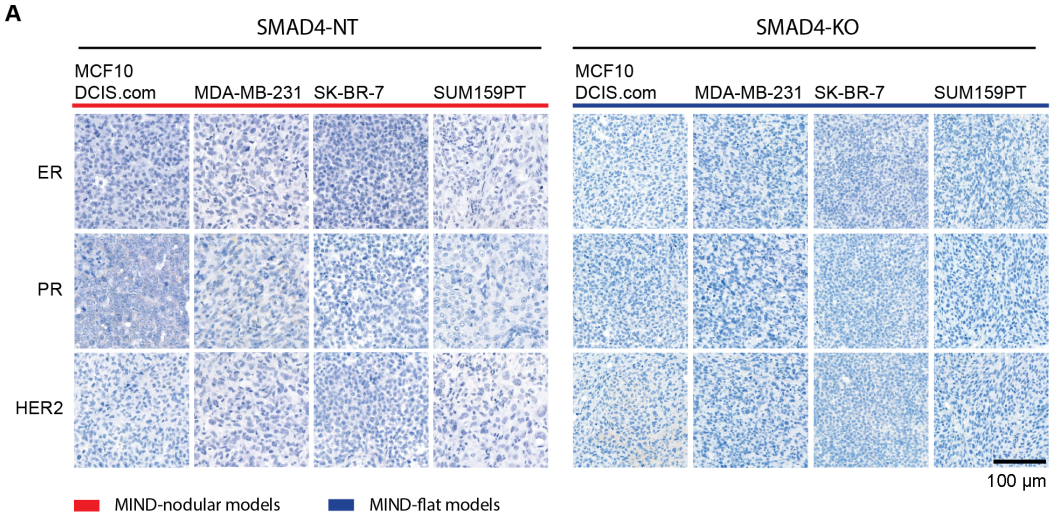

B

	Cell line	ER	PR	HER2
SMAD4-NT	MCF10DCIS.com	-	-	-
	MDA-MB-231	-	-	-
	SK-BR-7	-	-	-
	SUM159PT	-	-	-
SMAD4-KO	MCF10DCIS.com	-	-	-
	MDA-MB-231	-	-	-
	SK-BR-7	-	-	-
	SUM159PT	-	-	-

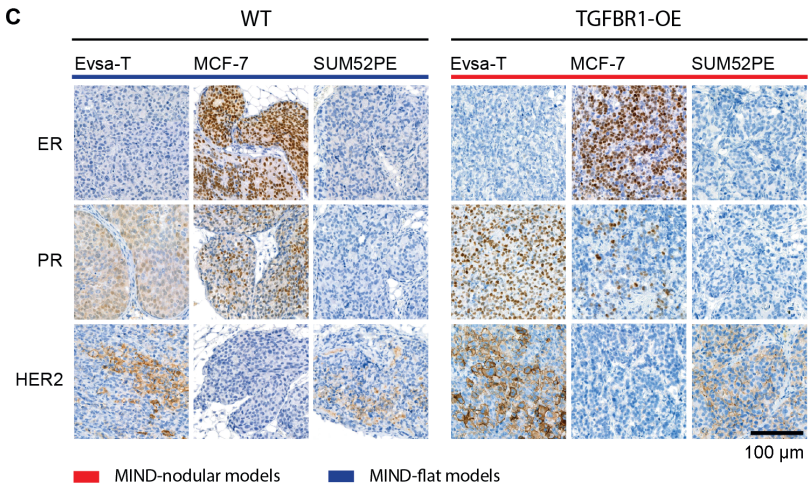

D

	Cell line	ER	PR	HER2
WT	Evsa-T	-	+	+
	MCF-7	+	+	-
	SUM52PE	-	-	+
TGFBR1-OE	Evsa-T	-	+	+
	MCF-7	+	+	-
	SUM52PE	-	-	+

Supplementary Figure 14: Tumour IHC subtype is not affected by SMAD4-KO or TGFBR1-OE

A) Representative IHC staining of ER, PR, and HER2 of MIND-nodular tumours from SMAD4-WT cell transplants compared to MIND-flat SMAD4-KO transplants (scale bar 100 µm). **B**) ER, PR, and HER2 assessment based on IHC of SMAD4-NT and SMAD4-KO tumours. **C**) Representative IHC staining of ER, PR, and HER2 of MIND-flat tumours from TGFBR1-WT cell transplants compared to MIND-nodular TGFBR1-OE transplants (scale bar 100 µm). **D**) ER, PR, and HER2 assessment based on IHC of WT and TGFBR1-OE tumours.